



HAL
open science

Tectonic record, magmatic history and hydrothermal alteration in the Hercynian Guérande leucogranite, Armorican Massif, France

Christophe Ballouard, Philippe Boulvais, Marc Poujol, Denis Gapais, Philippe Yamato, Romain Tartese, Michel Cuney

► To cite this version:

Christophe Ballouard, Philippe Boulvais, Marc Poujol, Denis Gapais, Philippe Yamato, et al.. Tectonic record, magmatic history and hydrothermal alteration in the Hercynian Guérande leucogranite, Armorican Massif, France. *Lithos*, 2015, 220-223, pp.1-22. 10.1016/j.lithos.2015.01.027. insu-01118586

HAL Id: insu-01118586

<https://insu.hal.science/insu-01118586>

Submitted on 27 Jun 2024

HAL is a multi-disciplinary open access archive for the deposit and dissemination of scientific research documents, whether they are published or not. The documents may come from teaching and research institutions in France or abroad, or from public or private research centers.

L'archive ouverte pluridisciplinaire **HAL**, est destinée au dépôt et à la diffusion de documents scientifiques de niveau recherche, publiés ou non, émanant des établissements d'enseignement et de recherche français ou étrangers, des laboratoires publics ou privés.

Manuscript Number: LITHOS4479R2

Title: Tectonic record, magmatic history and hydrothermal alteration in the Hercynian Guérande leucogranite, Armorican Massif, France.

Article Type: Regular Article

Keywords: leucogranite petrogenesis, geochemistry, geochronology, structure, Hercynian, Armorican Massif

Corresponding Author: Mr. Christophe Ballouard, MSc.

Corresponding Author's Institution: University Rennes 1

First Author: Christophe Ballouard, MSc.

Order of Authors: Christophe Ballouard, MSc.; Philippe Boulvais, PhD; Marc Poujol, PhD; Denis Gapais, PhD; Philippe Yamato, PhD; Romain Tartèse, PhD; Michel Cuney, PhD

Abstract: The Guérande peraluminous leucogranite was emplaced at the end of the Carboniferous in the southern part of the Armorican Massif. At the scale of the intrusion, this granite displays structural heterogeneities with a weak deformation in the southwestern part, whereas the northwestern part is marked by the occurrence of S/C and mylonitic extensional fabrics. Quartz veins and pegmatite dykes orientations as well as lineations directions in the granite and its country rocks demonstrate both E-W and N-S stretching. Therefore, during its emplacement in a extensional tectonic regime, the syntectonic Guérande granite has probably experienced some partitioning of the deformation. The southwestern part is characterized by a muscovite-biotite assemblage, the presence of restites and migmatitic enclaves, a low abundance of quartz veins compared to pegmatite dykes. In contrast, the northwestern part is characterized by a muscovite-tourmaline assemblage, evidence of albitization and gresenization and a larger amount of quartz veins. The southwestern part is thus interpreted as the feeding zone of the intrusion whereas the northwestern part corresponds to its apical zone. The granite samples display continuous compositional evolutions in the range 69.8 - 75.3 wt.% SiO₂. High initial ⁸⁷Sr/⁸⁶Sr ratios and low ϵ Nd(T) values suggest that the peraluminous Guérande granite (A/CNK > 1.1) was formed by partial melting of metasedimentary formations. Magmatic evolution was controlled primarily by fractional crystallization of K-feldspar, biotite and plagioclase (An₂₀). The samples from the apical zone show evidence of secondary muscovitization. They are also characterized by a high content in incompatible elements such as Cs and Sn, as well as low Nb/Ta and K/Rb ratios. The apical zone of the Guérande granite underwent a pervasive hydrothermal alteration during or soon after its emplacement. U-Th-Pb dating on zircon and monazite revealed that the Guérande granite was emplaced 309.7 ± 1.3 Ma ago and that a late magmatic activity synchronous with hydrothermal circulation occurred at ca. 303 Ma. These new structural, petrological and geochronological data presented for the Guérande leucogranite highlight the interplay between the emplacement in an extensional tectonic regime, magmatic differentiation and hydrothermal alteration, and provide a general background for the understanding of the processes controlling some mineralization in the western European Hercynian belt.

1 **Tectonic record, magmatic history and hydrothermal alteration in the Hercynian Guérande**
2 **leucogranite, Armorican Massif, France.**

3

4 Ballouard C. ^{*1}, Boulvais P. ¹, Poujol M. ¹, Gapais D. ¹, Yamato P. ¹, Tartèse R. ², Cuney M. ³

5 ¹ UMR CNRS 6118, Géosciences Rennes, OSUR, Université, Rennes 1, 35042 Rennes Cedex,
6 France)

7 ² Planetary and Space Sciences, The Open University, Walton Hall - Milton Keynes, MK7
8 6AA, UK

9 ³ GeoRessources UMR 7359, CREGU, Campus Sciences-Aiguillettes BP 70239, 54506
10 Vandoeuvre-lès-Nancy, France

11

12 *corresponding author. Tel: +33 223 23 30 81.

13 E mail adress: christophe.ballouard@univ-rennes1.fr

14

15

16 **Key words:** leucogranite petrogenesis, geochemistry, U-Th-Pb LA-ICP-MS geochronology,
17 structure, Hercynian, Armorican Massif

18

19 **Abstract**

20 The Guérande peraluminous leucogranite was emplaced at the end of the Carboniferous in the
21 southern part of the Armorican Massif. At the scale of the intrusion, this granite displays structural
22 heterogeneities with a weak deformation in the southwestern part, whereas the northwestern part is
23 marked by the occurrence of S/C and mylonitic extensional fabrics. Quartz veins and pegmatite dykes
24 orientations as well as lineations directions in the granite and its country rocks demonstrate both E-W
25 and N-S stretching. Therefore, during its emplacement in a extensionnal tectonic regime, the
26 syntectonic Guérande granite has probably experienced some partitioning of the deformation. The
27 southwestern part is characterized by a muscovite-biotite assemblage, the presence of restites and
28 migmatitic enclaves, a low abundance of quartz veins compared to pegmatite dykes. In contrast, the
29 northwestern part is characterized by a muscovite-tourmaline assemblage, evidence of albitization and
30 gresenization and a larger amount of quartz veins. The southwestern part is thus interpreted as the

31 feeding zone of the intrusion whereas the northwestern part corresponds to its apical zone. The granite
32 samples display continuous compositional evolutions in the range 69.8 – 75.3 wt.% SiO₂. High initial
33 ⁸⁷Sr/⁸⁶Sr ratios and low ε_{Nd}(T) values suggest that the peraluminous Guérande granite (A/CNK > 1.1) was
34 formed by partial melting of metasedimentary formations. Magmatic evolution was controlled primarily
35 by fractional crystallization of K-feldspar, biotite and plagioclase (An₂₀). The samples from the apical
36 zone show evidence of secondary muscovitization. They are also characterized by a high content in
37 incompatible elements such as Cs and Sn, as well as low Nb/Ta and K/Rb ratios. The apical zone of the
38 Guérande granite underwent a pervasive hydrothermal alteration during or soon after its emplacement.
39 U-Th-Pb dating on zircon and monazite revealed that the Guérande granite was emplaced 309.7 ± 1.3
40 Ma ago and that a late magmatic activity synchronous with hydrothermal circulation occurred at ca. 303
41 Ma. These new structural, petrological and geochronological data presented for the Guérande
42 leucogranite highlight the interplay between the emplacement in an extensional tectonic regime,
43 magmatic differentiation and hydrothermal alteration, and provide a general background for the
44 understanding of the processes controlling some mineralization in the western European Hercynian belt.
45

46 **1. Introduction**

47 Peraluminous leucogranites are widespread throughout orogenic belts especially those associated
48 with continental collision (Barbarin, 1999). They formed mostly by partial melting of metasedimentary
49 rocks buried at low crustal depths (Lefort et al., 1987; Puziewicz and Johannes, 1988; Patiño Douce and
50 Johnston, 1991; Patiño Douce, 1999), while their exhumation within the crust is generally favored by
51 crustal-scale faults or shear zones (Hutton, 1988; D'lemos et al., 1992; Collins and Sawyer, 1996; Searle,
52 1999). Peraluminous leucogranite can display geochemical heterogeneities from the sample scale to
53 that of the magmatic chamber. These variations can reflect several processes such as progressive partial
54 melting, partial melting of heterogeneous metasedimentary sources (Deniel et al., 1987; Brown and
55 Pressley, 1999), variable degree of entrainment of peritectic assemblages (Stevens et al., 2007; Clemens
56 and Stevens, 2012), entrainment of unmelted restite (Chappell et al., 1987), magma mixing (Słaby and

57 Martin, 2008), wall rock assimilation (Ugidos and Recio, 1993) and fractional crystallization (e.g. Tartèse
58 and Boulvais, 2010).

59 During the magma ascent and its final crystallization at the emplacement site, magmatic fluids may
60 exsolve from the melt and give rise to numerous pegmatite and quartz veins. Alteration induced by the
61 pervasive circulation of fluids in the late stage of the leucogranites evolution can induce consequent
62 element mobility (Dostal and Chatterjee, 1995; Förster et al., 1999; Tartèse and Boulvais, 2010).

63 In the Hercynian belt, peraluminous leucogranites are mostly Carboniferous in age (Bernard-Griffiths
64 et al., 1985; Lagarde et al., 1992). They are present throughout the belt in the Bohemian Massif (Förster
65 et al., 1999), in Cornwall (Willis-Richards and Jackson, 1989; Chen et al., 1993), in the Iberian Massif
66 (Capdevila et al., 1973) as well as in the French Armorican and Central Massifs (Lameyre et al., 1980; La
67 Roche et al., 1980; Bernard-Griffiths et al., 1985, Tartese et al., 2011a, b).

68 In the Armorican Massif, the peraluminous leucogranites are syntectonic (Cogné, 1966; Jégouzo,
69 1980) and mostly located in its southern part. They are closely associated with either strike-slip
70 lithospheric shear zones, the so-called “South Armorican Shear Zone” (Berthé et al., 1979; Strong and
71 Hanmer, 1981; Tartèse and Boulvais, 2010), or with extensional shear zones (Gapais, et al., 1993 ;
72 Turrillot et al., 2009).

73 The Guérande granite is one of the leucogranites emplaced in an extensional deformation zone
74 during the Carboniferous synconvergence extension of the internal zone of the Hercynian belt (Gapais et
75 al, 1993). The Guérande granite offers a unique opportunity to characterize the internal differentiation
76 of a granitic pluton, and to study the relationships between crustal magmatism and (i) regional tectonics
77 and (ii) fluid driven alteration, in the heart of the Hercynian belt. The purpose of this paper is therefore
78 to address these different issues, based on new field descriptions and new petrological, geochemical
79 and geochronological data. These data are the first obtained for this strategic intrusion over the last
80 thirty years (Bouchez et al., 1981; Ouddou, 1984).

81

82 **2. Geological setting**

83 *2.1. The South Armorican Massif*

84 The southern part of the Armorican Massif (Fig. 1) belongs to the internal zone of the Hercynian
85 orogenic belt of Western Europe. It is bounded to the north by the South Armorican Shear Zone (SASZ),
86 a lithospheric dextral strike-slip shear zone divided into two branches (Gumiaux et al., 2004). From top
87 to bottom, three main tectono-metamorphic units can be structurally distinguished in the South
88 Armorican domain (Fig. 1):

- 89 - High Pressure-Low Temperature units, represented at the top of the pile by the blueschist klippen
90 of the Groix island and the Bois-de-Cené (1.4-1.8 GPa, 500-550°C, Bosse et al., 2002) and at the
91 bottom by the Vendée Porphyroid Nappe made of metamorphosed metavolcanics and black
92 shales (0.8 GPa, 350-400°C; Le Hébel et al., 2002). Ductile deformations, metamorphism and
93 exhumation of these units relate to early tectonic events, around 360 Ma (Bosse et al., 2005)
- 94 - Intermediate units mostly made of micaschists affected by a Barrovian metamorphism from
95 greenschist to amphibolite facies conditions (Bossière, 1988; Triboulet and Audren, 1988;
96 Goujou, 1992)
- 97 - Lower units constituted by high grade metamorphic rocks comprising gneiss, granitoids and
98 abundant migmatites related to metamorphism with PT condition of 0.8 GPa, 700-750°C (Jones
99 and Brown, 1990).

100 The Barrovian metamorphism developed during crustal thickening and was followed by a major
101 extensional shearing event that occurred during Upper Carboniferous, around 310 Ma (Gapais et al., in
102 press; Gapais, et al., 1993; Burg et al., 1994; Cagnard et al., 2004). Crustal extension was accompanied
103 by the exhumation and the rapid cooling of migmatites (about 40°C per Ma; Jones and Brown, 1990;
104 Gapais et al., 1993). At a regional scale, the structural patterns can be described as lower crustal,
105 migmatite-bearing, extensional domes, covered by micaschist units and overlying HP-LT units that
106 belonged to the upper brittle crust during the Upper Carboniferous extension.

107 Several leucogranites (Quiberon, Sarzeau, Guérande) are intrusive within the micaschists, above
108 migmatite bearing units and below the contact with the porphyroids (Fig. 1 and Fig. 2). On the basis of
109 structural features and geochronological works, it has been argued that these granites were emplaced

110 during the Upper Carboniferous extension (Gapais et al., 1993; Gapais et al., in press; Le Hébel, 2002;
111 Turrillot et al., 2009).

112 Several leucogranite intrusions occur also along the SASZ (Berthé et al., 1979) and present S/C
113 structures which indicate syn-cooling shearing (Gapais, 1989). Among them, the Questembert and Lizio
114 granites (Fig. 1), that have been dated at 316 ± 3 Ma (Tartèse et al., 2011b) and 316 ± 6 Ma (Tartèse et
115 al., 2011a) respectively, were formed by the partial melting of Upper Proterozoic metasediments, and
116 shared a similar magmatic history, marked by the fractionation of feldspar and biotite together with the
117 zircon and monazite grains included in biotite (Tartèse and Boulvais, 2010).

118 Some giant quartz veins are also located along the SASZ, in a network of regionally distributed
119 vertical fractures oriented N160°. Isotopic and fluid inclusions studies suggest that the fluids involved
120 originated both from the exhuming lower crust and downward meteoric circulation (Lemarchand et al.,
121 2012). These authors interpreted these veins as giant tension gashes and proposed that these veins
122 attest for crustal-scale fluid circulation during the exhumation of the lower crust and the concomitant
123 regional strike-slip deformation.

124

125 *2.2. Previous studies on the Guérande granite*

126 The Guérande leucogranite (Fig. 2 and Fig. 3), a ca. 1 kilometer thick 3-D blade shaped structure
127 dipping slightly northward (Vignerresse, 1983; Bouchez et al., 1981), was emplaced along an extensional
128 deformation zone (Gapais et al., 1993). To the north, the granite presents an abrupt contact with
129 micaschists and metavolcanics that recorded a contact metamorphism as demonstrated by the presence
130 of staurolite and garnet (Valois, 1975). To the southwest, the contact is different and presents a
131 progressive evolution with the Saint-Nazaire migmatites, which may represent the source of the
132 Guérande granite (Bouchez et al., 1981). Several enclaves of micaschists occur within the granite and a
133 “kilometer-size” body of isotropic subfacies crosscuts its southwestern edge (Fig. 2 and Fig. 3). Within
134 the granite, the foliations are generally weakly expressed and basically of magmatic type. They dip
135 generally 20-30° northward and bear weak dip-slip mineral lineations (Fig. 2). The southwestern part of
136 the intrusion is also characterized by magmatic- or migmatitic-like foliations and mineral lineations. In

137 contrast, S/C fabrics affect its northern edge (Bouchez et al., 1981). The occurrences of migmatites to
138 the south, below the intrusion, and of micaschists to the north above it, underline that the
139 southwestern part corresponds to the base of the granite and the northwestern part to its roof
140 (Bouchez et al., 1981). By shearing, the top-to-the-north extensional deformation zone (Fig. 2 and Fig. 3)
141 likely induced translation of the upper part of the granitic body. As a consequence, both the root zone in
142 the southwestern part and the apical zone in the northwestern part are exposed to the surface today.
143 The general shape of the intrusion as it appears today (thin laccolith intrusion with a large horizontal
144 extension) likely relates to this peculiar tectonic context at the time of emplacement.

145 A fluid-inclusions study performed on quartz veins occurring near the roof of the Guérande granite
146 reveals that it was probably emplaced at shallow depth (around 3 km; Le Hébel et al., 2007). An
147 extensional graben (the so-called “Piriac synform”; Valois, 1975), where rocks from the HP-LT upper unit
148 (Vendée porphyroid unit) crop out (Fig. 3), affects the northwestern part of the granite. Valois (1975)
149 and Cathelineau(1981) interpreted this structure as the result of roof collapse of the intrusion.

150 Although its age is not well constrained yet, the Guérande granite was emplaced during the Upper
151 Carboniferous: muscovite $^{40}\text{Ar}/^{39}\text{Ar}$ data yielded dates of 307 ± 0.3 Ma for an undeformed sample that
152 could be interpreted as a cooling age and 304 ± 0.6 Ma for a mylonitized sample which could represent
153 the age of the deformation (Le Hébel, 2002). Le Hébel (2002) also reported $^{40}\text{Ar}/^{39}\text{Ar}$ dates of 303.3 ± 0.5
154 Ma obtained on muscovite grains from a quartz vein intrusive within the Guérande granite and $303.6 \pm$
155 0.5 Ma for a sheared granite sample.

156

157 **3. Field description and sampling**

158 Since the Guérande granite is largely covered by salt marsh (Fig. 2), it crops out only in a few inland
159 quarries and along the coastline. Overall, these coastal outcrops are of good quality and are therefore
160 suitable for establishing cross sections from the southwestern to the northwestern parts of the
161 intrusion.

162

163 *3.1. Petrographic zonation within the Guérande granite*

164 At the scale of the intrusion, the Guérande granite displays petrographic heterogeneities with
165 variable proportions of muscovite, biotite and tourmaline (Fig. 2). The southwestern part of the pluton is
166 characterized by a muscovite-biotite assemblage (Fig. 4a) whereas the northwestern part is
167 characterized by a muscovite-tourmaline assemblage (Fig. 4b). Moreover, numerous meter-size zones of
168 isotropic granite (I granite in Fig. 4c), as well as enclaves of restites and migmatites are present in the
169 southwestern part of the granite, whereas greisens and albitized rocks occur in the northwestern part
170 (Fig. 2). These observations, together with the fact that the foliation dips northward, are consistent with
171 the zonation of the pluton, the southwestern part corresponding to the feeding zone of the granite
172 whereas the northwestern part corresponds to the apical zone which typically concentrates the
173 hydrothermal activity.

174 3.2. Structures and dykes

175 The central and southwestern parts of the intrusion display magmatic and roughly defined foliations
176 (Fig. 4a and d) whereas S/C structures and mylonites (Fig. 4e) occur along the northern edge. This strain
177 localization, responsible for the development of solid state fabrics, occurred to the north, at the roof of
178 the pluton, in association with the extensional deformation zone which caps the Guérande granite (Fig.
179 2 and Fig. 3).

180 In the granite, the lineation dips generally northward but a significant scattering exists (Fig. 2). To
181 the northwest, at the roof of the granite, dip-slip type lineations (Fig. 5a) associated with top to the
182 north S/C fabrics occur. However, the adjacent country-rocks show evidence of E-W stretching, with
183 outcrop-scale tilted blocks and rocks affected by a contact metamorphism bearing E-W elongated
184 patches of retrogressed cordierite (Fig. 5b).

185 Many pegmatitic dykes (Fig. 4c) together with a few aplitic dykes and quartz veins (Fig. 4f) crosscut
186 the Guérande granite. To the north-west, pegmatites are biotite-free and contain muscovite \pm
187 tourmaline whereas, to the south-west, the pegmatites are biotite-bearing. These differences in the
188 pegmatite compositions mimic the petrographic heterogeneities previously described for the pluton
189 (i.e., biotite is absent to the north-west and present to the south-west while tourmaline appears only in
190 the northwestern part of the intrusion). Figure 5 shows the strike directions for 180 of these dykes and

191 veins in three different locations. In the northernmost area (Piriac) located close to the roof of the
192 intrusion and associated, in part, with the mylonitized granite (Fig. 4e), the pegmatites contain a Qtz-
193 Fsp-Ms assemblage. Quartz veins are less present than pegmatites (Fig. 5c). The strike of the dykes and
194 veins in this zone is mostly oriented N110°-N140° and is nearly perpendicular to the strike of the
195 lineation recorded in the granite. Further to the south, close to La Turballe, pegmatitic dykes contain a
196 Qtz-Fsp-Ms±Turm assemblage. The proportion of pegmatite dykes over quartz veins (Fig. 5d) is
197 comparable to that in Piriac. In this area, dykes are mainly oriented N160°-N170° and are slightly oblique
198 to the strike of the lineation in the granite. In the southernmost area (Le Croisic), pegmatite dykes
199 contain a Qtz-Fsp-Ms±Bt assemblage and appear in a greater proportion than quartz veins (Fig. 5e).
200 Dykes in this zone strike dominantly N000°-N020°, i.e. roughly parallel to the strike of the lineation in
201 the granite. In most parts of the intrusion, the dykes and veins record an E-W stretching, which is
202 different from that recorded by the granite itself, although a significant scattering of the lineations is
203 observed (Fig. 2).

204

205 3.3. *Sampling and samples*

206 A sampling strategy was developed in order to take into account the petrographic variability
207 observed in the field at the scale of the intrusion. For this purpose, we targeted all the inland ancient
208 quarries in addition to the outcrops available along the coast. A total of 21 samples were collected.

209 All the samples contain a Qtz-Kfs-Pl-Ms assemblage (Fig. 6a) with a variable amount of Bt and Turm.
210 Quartz is normally anhedral, commonly forms polycrystalline cluster (Fig. 6b) and some grains show
211 undulose extinction characteristic of intracrystalline deformation. The alkali feldspar is generally
212 anhedral and some grains display Carlsbad twinning and rare string-shaped sodic perthitic exsolutions.
213 The plagioclase is anhedral to sub-euhedral, shows polysynthetic twinning and can be associated with
214 myrmekites. Muscovite is generally euhedral, flake shaped and occur also with a fish-like habit (Ms I in
215 Fig. 6c). Fine-grained secondary muscovite can be abundant in some facies. It developed as sericite
216 inclusion in feldspar, as small grains around coarse primary muscovite or within foliation planes (Ms II in
217 Fig. 6c). Biotite is brown, sub-euhedral to euhedral and commonly appears as intergrowth within

218 muscovite flakes (Fig. 6b). Biotite hosts most of the accessory minerals such as apatite, Fe-Ti oxide,
219 zircon and monazite (Fig. 6a).

220 The 21 samples have been divided into five different groups, based on their respective petrographic
221 characteristics (see Table 1, and sample location on Fig. 2):

222 (1) The *root facies* (southern part of the intrusion) is heterogeneous and includes facies marked by
223 a roughly defined foliation (Fig. 4a and d) and zones of fine- to medium-grained isotropic
224 granites (0.5 – 3 mm; Fig. 4c). In the root facies, muscovite is normally more abundant than
225 biotite and this facies contains numerous accessory minerals (Fe-Ti oxide, apatite, zircon and
226 monazite) (Fig. 6a). Small garnet grains occur in sample GUE-17 (Table 1).

227 (2) The *Ms-Bt coarse- to medium-grained granite* (3-5 mm) represents the most common facies in
228 the intrusion. The muscovite is commonly coarse (> 1 mm) and is more abundant than biotite
229 (<1 mm, Fig. 6b). Fine secondary muscovite (< 1 mm) is rarely observed inside the foliation.

230 (3) The *Ms-Turm coarse- to medium-grained granite* (3-5 mm) occurs only in the northwestern part
231 of the intrusion (apex, Fig. 2). Tourmaline (<5%) is normally several millimeters long, green
232 brown in color, presents coarse cracks and hosts inclusions of quartz and feldspar. Fine
233 secondary muscovite (<1mm) is abundant in this facies (Fig. 6c) where it occurs inside foliation
234 planes or around coarse primary muscovite flakes (>1mm). Biotite is rare and generally appears
235 as inclusions inside primary muscovite crystals (Fig. 6c).

236 (4) The *Ms-Bt fine-grained granite* (0.5-2 mm) occurs mainly near La Turballe and in the
237 northeastern extremity of the intrusion. Ouddou (1984) has reported some occurrences of this
238 facies in the eastern and the southwestern parts. Bouchez et al (1981) interpreted this facies as
239 kilometer thick dykes (Fig. 3), but the existence of mingling features at the contact between this
240 fine-grained facies and the coarse- to medium-grained granites suggests that they are
241 contemporaneous (Ouddou, 1984). In this granite, perthitic orthoclase is common and
242 muscovite is more abundant than biotite. This facies contains numerous monazite grains.

243 (5) *Granitic meter-thick dykes* have been sampled in different locations within the intrusion. They
244 normally show similar mineralogical and textural features, and commonly display an aplitic
245 texture (Table 1).

246

247 Chloritization, albitization and greisenization occur at different locations in the Guérande intrusion
248 (Table 1 and Fig. 2). Chloritization of biotite is visible at the microscopic scale and is localized to the
249 northern central part of the granite (Fig. 2). The chlorite commonly hosts small (< 50 µm) highly
250 pleochroic anhedral grains, likely anatase. Albitization is linked to shear zones and results in a greater
251 proportion of albite relative to quartz and micas; it may be discrete (sample GUE 2) or more intense
252 (sample GUE 19a). Garnet is present in the albitized sample GUE-19a (Table 1). Meter-scale
253 greisenization occurs and both albitization and greisenization are restricted to the northwestern part of
254 the Guérande granite (Fig. 2).

255

256 **4. Analytical techniques**

257 *4.1. Mineral compositions*

258 Mineral compositions were measured using a Cameca SX-100 electron microprobe at IFREMER,
259 Plouzané, France. Operating conditions were a 15 kV acceleration voltage, a beam current of 20 nA and
260 a beam diameter of 5 µm. Counting times were approximately 13–14 s. For a complete description of
261 the analytical procedure and the list of the standards used, see Pitra et al. (2008).

262 *4.2. Major and trace-elements analyses*

263 Large samples (5 to 10 kg) were crushed following a standard protocol to obtain adequate powder
264 fractions using agate mortars. Chemical analyses were performed by the Service d'Analyse des Roches
265 et des Minéraux (SARM; CRPG-CNRS, Nancy, France) using a ICP-AES for major-elements and a ICP-MS
266 for trace-elements following the techniques described in Carignan et al. (2001)

267 *4.3. Isotopic analyses*

268 Sm-Nd and Sr isotopic values were determined on whole-rock samples. All the analyses were
269 carried out at the Géosciences Rennes Laboratory using a 7 collectors Finnigan MAT-262 mass

270 spectrometer. Samples were spiked with a ^{149}Sm - ^{150}Nd and ^{84}Sr mixed solution and dissolved in a HF-
271 HNO_3 mixture. They were then dried and taken up with concentrated HCl. In each analytical session, the
272 unknowns were analyzed together with the Ames Nd-1 Nd or the NBS-987 Sr standards, which during
273 the course of this study yielded an average of 0.511956 (± 5) and 0.710275 (± 10) respectively. All the
274 analyses of the unknowns have been adjusted to the long-term value of $^{143}\text{Nd}/^{144}\text{Nd}$ value of 0.511963
275 for Ames Nd-1 and reported $^{87}\text{Sr}/^{86}\text{Sr}$ values were normalized to the reference value of 0.710250 for
276 NBS-987. Mass fractionation was monitored and corrected using the value $^{146}\text{Nd}/^{144}\text{Nd} = 0.7219$ and
277 $^{88}\text{Sr}/^{86}\text{Sr} = 8.3752$. Procedural blanks analyses yielded values of 400 pg for Sr and 50 pg for Nd and are
278 therefore considered to be negligible.

279 *4.4. U-Th-Pb analyses*

280 A classic mineral separation procedure has been applied to concentrate minerals suitable for U-Th-
281 Pb dating using the facilities available at Géosciences Rennes. Rocks were crushed and only the powder
282 fraction with a diameter $< 250 \mu\text{m}$ has been kept. Heavy minerals were successively concentrated by
283 Wilfley table and heavy liquids. Magnetic minerals were then removed with an isodynamic Frantz
284 separator. Zircon and monazite grains were carefully handpicked under a binocular microscope and
285 embedded in epoxy mounts. The grains were then hand-grounded and polished on a lap wheel with a 6
286 μm and 1 μm diamond suspension successively. Zircon grains were imaged by cathodoluminescence (CL)
287 using a Reliotron CL system equipped with a digital color camera available in Géosciences Rennes,
288 whereas monazite grains were imaged using the electron microprobe facility in IFREMER, Brest.

289 U-Th-Pb geochronology of zircon and monazite was conducted by in-situ laser ablation inductively
290 coupled plasma mass spectrometry (LA-ICPMS) at Géosciences Rennes using a ESI NWR193UC excimer
291 laser coupled to a quadrupole Agilent 7700x ICP-MS equipped with a dual pumping system to enhance
292 sensitivity. The instrumental conditions are reported in Table 2.

293 The ablated material was carried into helium, and then mixed with nitrogen and argon, before
294 injection into the plasma source. The alignment of the instrument and mass calibration was performed
295 before each analytical session using the NIST SRM 612 reference glass, by inspecting the ^{238}U signal and
296 by minimizing the ThO^+/Th^+ ratio ($< 0.5\%$). During the course of an analysis, the signals of $^{204}(\text{Pb}+\text{Hg})$,

297 ^{206}Pb , ^{207}Pb , ^{208}Pb and ^{238}U masses were acquired. The occurrence of common Pb in the sample can be
298 monitored by the evolution of the $^{204}(\text{Pb}+\text{Hg})$ signal intensity, but no common Pb correction was applied
299 owing to the large isobaric interference with Hg. The ^{235}U signal is calculated from ^{238}U on the basis of
300 the ratio $^{238}\text{U}/^{235}\text{U}=137.88$. Single analyses consisted of 20 s of background integration, followed by a 60
301 s integration with the laser firing and then a 10 s delay to wash out the previous sample. Ablation spot
302 diameters of 26-44 μm and 20 μm with repetition rates of 3-5 Hz and 1-2 Hz were used for zircon and
303 monazite, respectively. Data were corrected for U–Pb and Th–Pb fractionation and for the mass bias by
304 standard bracketing with repeated measurements of the GJ-1 zircon (Jackson et al., 2004) or the Moacir
305 monazite standards (Gasquet et al., 2010). Repeated analyses of 91500 (1061 ± 3 Ma ($n=20$);
306 (Wiedenbeck et al., 1995) or Manangoutry monazite (554 ± 3 Ma ($n=20$); Paquette and Tiepolo, 2007)
307 standards treated as unknowns were used to control the reproducibility and accuracy of the corrections.
308 Data reduction was carried out with the GLITTER[®] software package developed by the Macquarie
309 Research Ltd. (Jackson et al., 2004). Concordia ages and diagrams were generated using Isoplot/Ex
310 (Ludwig, 2001). All errors given in Supplementary Table 1 and 2 are listed at one sigma, but where data
311 are combined for regression analysis or to calculate weighted means, the final results are provided with
312 95% confidence limits.

313 **5. Mineralogical composition**

314 Five samples from the Guérande granite representative of the different petrographic varieties have
315 been selected for chemical analyses on feldspar, biotite and muscovite. These are two Ms-Bt coarse- to
316 medium-grained granite (GUE-3 and GUE-8), one Ms-Turm coarse- to medium-grained granite (GUE-1),
317 one Ms-Bt fine-grained granite (GUE-4) and one granitic dyke (GUE-5).

318

319 *5.1. Feldspar and biotite (Supplementary Table 3)*

320 Plagioclase chemical compositions display a well-defined trend in the Ab-An-Or ternary diagram (Fig.
321 7a). The plagioclase calcium contents decrease from the Ms-Bt fine-grained granite (GUE-4; $\text{An} = 0.09$)
322 to the Ms-Turm coarse- to medium-grained granite (GUE-1; $\text{An} = 0.02$), whereas the Ms-Bt coarse- to

323 medium-grained granites and the dyke display intermediate contents ($An = 0.07-0.05$). In alkali feldspar,
324 the potassium content is merely constant ($Or = 0.90 - 0.93$) irrespective of the petrographic facies.

325 Biotite displays typical chemical composition for peraluminous granites with an elevated content in
326 Al ($Al_{TOT} > 3.5$ pfu; Nachit et al., 1985) and $X_{Mg} = 0.27 - 0.28$. GUE-3 displays a lower Mg content ($X_{Mg} =$
327 0.22).

328

329 *5.2. Muscovite (Supplementary Table 4)*

330 Muscovite grains in the Ms-Bt fine-grained granite (GUE-4) and the granitic dyke (GUE-5) fall in the
331 primary muscovite field defined by Miller et al. (1981) and display homogenous Mg content (Fig. 7b).
332 The Mg content of the muscovite grains increases in the other samples and the secondary affinity of
333 muscovite tends to increase from the Ms-Bt coarse- to medium-grained granites (GUE-3 and 8) to the
334 Ms-Turm coarse- to medium-grained granite (GUE-1, Fig. 7b). In these samples, several grains of coarse
335 muscovite display heterogeneous Mg contents: the cores are poorer in Mg and belong to the primary
336 muscovite field whereas their rims are richer in Mg and fall in the secondary muscovite field (Fig. 7b).
337 Regarding the small muscovite grains present in the foliation (labeled MsII in Figure 6c), they all plot in
338 the secondary field.

339

340 **6. Whole-rock geochemistry**

341 *6.1. Major elements (Table 3)*

342 The chemical diagram of Hughes (1973) is useful to identify magmatic rocks that have undergone
343 metasomatism, which may be responsible for the loss of their initial igneous composition. In this
344 diagram (Fig. 8a), three samples fall outside or at the limit of the field for igneous rocks. These are the
345 two samples from the aplite dyke GUE-19a and GUE-19b and a Ms-Turm coarse- to medium-grained
346 granite (sample GUE-21). The chemical mineralogical Q-P diagram (Debon and Le Fort, 1988) is suitable
347 to evidence the mineralogical changes linked to chemical composition modification in igneous rocks
348 because it is sensitive to the proportion of quartz (Q parameter) and to the proportion of alkali feldspar
349 relative to plagioclase (P parameter). In this diagram (Fig. 8b), samples GUE-19a and GUE-19b display a

350 trend characteristic of an albitic alteration where albitization and dequartzification are associated with
351 the neoformation of albite. Samples GUE-2 and 20 display weak albitization. Sample GUE-21 displays
352 dequartzification associated with the neoformation of alkali feldspar. These results are consistent with
353 field and petrographic descriptions, which indicate that albitization affected samples GUE-19 and GUE-2
354 whereas greisens occur in the vicinity of sample GUE-21 (Fig. 2 and Table 1). According to the Hughes
355 and Q-P diagrams (Fig. 8a and b), the Guérande granite samples can be divided into two groups: the
356 unaltered samples, which display igneous compositions and the altered samples GUE-19 and GUE-21
357 that show evidence of hydrothermal alteration.

358 Similarly to some neighboring granites such as the Questembert and Lizio leucogranites (Tartèse and
359 Boulvais, 2010), all the unaltered samples from the Guérande granite display a peraluminous affinity in
360 the A/NK vs A/CNK diagram (A/CNK values ranging from 1.11 to 1.29; Fig. 8c and Table 3). However, the
361 altered sample GUE-19a shows A/CNK and A/NK values close to 1, which is typical for an albitized
362 granite (Boulvais et al., 2007) and reflects the disappearance of muscovite during albitization.

363 As shown in Figure 9a, unaltered samples display high SiO₂ contents ranging from 71.6 wt.% (GUE-
364 15) to 75.3 wt.% (GUE-20). The altered sample GUE-21 yields a low SiO₂ content of 69.8 wt.% whereas
365 albitized samples show high SiO₂ contents of 73.5 to 74.4 wt.%. Most of the major elements for the
366 unaltered samples display well defined evolution trends with increasing SiO₂, i.e., decreasing K₂O, CaO
367 and Fe₂O₃+MgO+TiO₂ contents whereas Na₂O content increases. Conversely, the altered samples rarely
368 follow these trends (Fig. 9a).

369 6.2. Trace-elements (Table 3)

370 Whereas some incompatible trace-elements such as Rb, Cs, W, U or Sn are not correlated with SiO₂,
371 several other trace-elements from the unaltered samples display well-defined evolution trends and
372 show large variations against SiO₂. Sr and Ba mimic the trends defined by K₂O, CaO and Fe₂O₃+MgO+TiO₂
373 (Fig. 9a). Zr, Th and La are also inversely correlated with SiO₂ and they decrease respectively from 81 to
374 13 ppm, 9.2 to 0.3 ppm and 19.1 to 1.3 ppm (Fig. 9a). Zr correlates well with Fe₂O₃+TiO₂+MgO while a
375 very good correlation exists between Zr, Th and La (Fig. 9b). Among altered samples, GUE-21 does not
376 follow the general trend provided by the unaltered samples in the Harker diagrams reported in function

377 of SiO₂ (Fig. 9a). Nevertheless, sample GUE-21 is indistinguishable from unaltered samples in the
378 diagrams involving Zr, La and Th (Fig. 9b). Samples GUE-19a and GUE-19b plot at the lower extremity of
379 these trends (Fig. 9b). GUE-19a, 19b and 20 are highly enriched in Be when compared to the other
380 samples (Be>120ppm).

381 The REE patterns obtained on the unaltered samples are somewhat variable (Fig. 10), show high
382 fractionation ((La/Lu)_N =10.8-28) and display either positive or negative Eu anomalies (Eu/Eu*=0.7-1.2),
383 the largest positive anomaly being recorded in the dyke sample GUE-5. These patterns are similar to
384 those obtained for the other Armorican Massif leucogranites (Bernard-Griffiths et al., 1985; Tartèse and
385 Boulvais, 2010). The aplite dyke GUE-20 is remarkable because of its large depletion in REE. Concerning
386 the altered samples, GUE-19a and GUE-19b show REE patterns similar to the ones from the aplite dyke
387 GUE-20. Sample GUE-21 displays a REE spectrum comparable with the other unaltered samples
388 suggesting that the REE distribution in this sample was not affected during fluid-rock interaction.

389 The evolution of some of the geochemical tracers sensitive to the interaction with fluids is reported
390 in Figure 11a with respect to the distance to the northwestern edge of the Guérande granite, identified
391 as the apical zone of the intrusion. In the apical zone, the Cs and Sn contents increase by about one
392 order of magnitude, from around 10 ppm to 100 ppm for both elements. This behavior is similar for Rb,
393 which increases from 200 to 450 ppm. Also, samples from the Guérande granite display fractionation of
394 the Nb/Ta ratios from about 6-8 down to about 2-4 in the apical zone, similarly to the hydrothermal
395 alteration trends identified in the nearby Questembert granite (Tartèse and Boulvais, 2010). Taking the
396 Cs content as a qualitative tracer for an increasing fluid-rock alteration (e.g. Förster et al., 1999; Fig.
397 11b), the Sn contents show a very well correlated evolution, whereas the Nb/Ta ratios are rather anti-
398 correlated with the Cs contents. Both trends are defined by the unaltered and altered samples.

399 **7. Radiogenic isotopes: Rb-Sr and Sm-Nd.**

400 Sr and Sm-Nd isotope analyses for some of the samples from the Guérande granite are reported in
401 Table 4 and Figure 12. Initial ⁸⁷Sr/⁸⁶Sr (I_{Sr}) and εNd(T) values have been recalculated for an age of 310 Ma
402 (see part 8). I_{Sr} values are high and vary from 0.7148 to 0.7197 while εNd(T) varies from -7.8 to -9.0. T_{DM}
403 values are old and vary from 1642 to 1736 Ma. In the εNd(T) vs I_{Sr} diagram (Fig. 12), a regional trend is

404 defined by the Rostrenen, Pontivy, Lizio, Questembert and Guérande peraluminous granites: $\epsilon\text{Nd}(T)$
405 values decrease while I_{sr} increases. This evolution may indicate an increase of crustal recycling going
406 southward in the southern part of the Armorican Massif as already noticed by Bernard-Griffiths et al.
407 (1985).

408 **8. Geochronology**

409 Sample GUE-3, a Ms-Bt coarse- to medium-grained granite collected in the northwestern part of the
410 intrusion (Fig. 2), provided both zircon and monazite grains. Thirty-six analyses were carried out on
411 nineteen zircon grains (Supplementary Table 1). The zircon population is characterized by translucent
412 colorless euhedral to sub-euhedral grains. Cathodoluminescence imaging reveals the presence of
413 inherited cores surrounded by zoned rims for most of the grains (Fig. 13a). They plot in a concordant to
414 discordant position (Fig. 14a) and yield $^{207}\text{Pb}/^{206}\text{Pb}$ dates ranging from 2604 ± 18 Ma down to 307 ± 27
415 Ma. A group of nine concordant to sub-concordant analyses allow to calculate a mean $^{206}\text{Pb}/^{238}\text{U}$ date of
416 309 ± 2.6 Ma (MSWD=1.0). The remaining 5 data (dashed line on Fig. 14a) plot in a sub-concordant to
417 discordant position and can be best explained by the presence of initial common Pb together with a
418 complex Pb loss.

419 In addition, sixteen monazite grains have also been analyzed (Supplementary Table 2). In a
420 $^{206}\text{Pb}/^{238}\text{U}$ vs. $^{208}\text{Pb}/^{232}\text{Th}$ concordia diagram, they plot in a concordant to sub-concordant position. All
421 sixteen analyses yield a mean $^{206}\text{Pb}/^{238}\text{U}$ date of 311.3 ± 2.2 Ma (MSWD=0.5) and the fifteen most
422 concordant analyses allow to calculate an equivalent (within error) concordia date of 309.4 ± 1.9 Ma
423 (MSWD=1.08).

424 Within the same facies (ie. Ms-Bt coarse- to medium-grained granite), a large zircon grain from
425 sample GUE-8 was analyzed. It displays well-defined magmatic zoning without any evidence of inherited
426 core (Fig. 13b). Eight analyses were performed and allow to calculate a poorly constrained concordia
427 date of 309.3 ± 6.1 Ma (MSWD=2.4) for the 6 most concordant points (not shown in this paper).

428 Zircon and monazite grains were also extracted from a third sample, GUE-4, a Ms-Bt fine grain
429 granite collected within the La Turballe quarry (Fig. 2). All the zircon grains were characterized by the
430 presence of cores and rims. Unfortunately, all the analyses performed on the zircon rims were

431 perturbed by a large amount of common Pb together with variable degrees of Pb loss. Furthermore
432 these zircon grains yielded uranium contents up to 20,000 ppm. Therefore, no ages could be calculated
433 from these zircon grains.

434 Forty-one analyses were carried out on twelve monazite grains. The monazite grains are rather large
435 (up to 300 micrometer), euhedral, and characterized by a Th distribution from heterogeneous (patchy)
436 to zoned (Fig. 13c) with a systematic Th enrichment around the edges of the grains. Independently from
437 where the spot analyses were located, all the acquired data are consistent and plot in a concordant to
438 sub-concordant position in a $^{206}\text{Pb}/^{238}\text{U}$ vs. $^{208}\text{Pb}/^{232}\text{Th}$ concordia diagram (Fig. 14c). Thirty-two
439 concordant analyses allow to calculate a concordia date of 309.7 ± 1.3 Ma (MSWD=0.81) which is
440 equivalent within error with a mean $^{206}\text{Pb}/^{238}\text{U}$ date of 310.9 ± 1.6 Ma (n=41; MSWD=1.3).

441 Finally, sample GUE-5 corresponds to a dyke intrusive into GUE-4. It provided abundant zircon and
442 monazite grains. Here again, all the zircon grains display cores and rims and all of them but one were
443 common-Pb rich and affected by variable degree of Pb loss. The only zircon that was not common-Pb
444 rich (Fig. 13d) yields a concordia date of 299.6 ± 5.4 Ma (MSWD =0.49) for the two analyses performed
445 in the rim.

446 Twenty-three analyses out of sixteen monazite grains were realized. They all plot in a concordant to
447 sub-concordant position in a $^{206}\text{Pb}/^{238}\text{U}$ vs. $^{208}\text{Pb}/^{232}\text{Th}$ concordia diagram (Fig. 14d). The eighteen most
448 concordant points yield a concordia date of 302.5 ± 1.6 Ma (MSWD=0.86), equivalent within error with a
449 mean $^{206}\text{Pb}/^{238}\text{U}$ date of 303.7 ± 1.7 Ma (MSWD=0.9) computed for all the analyses. These dates of 302.5
450 ± 1.6 Ma and 303.7 ± 1.7 Ma are equivalent within error with the Concordia date of 299.6 ± 5.4 Ma
451 obtained on the rim of the zircon grain.

452

453 **9. Discussion**

454 *9.1. Tectonic evolution*

455 The Guérande granite and its country rock record puzzling kinematic patterns which suggest a
456 particular deformation regime at the time of the granite emplacement.

457 First, to the northwest, S/C granites bear dip-slip type N-S lineation whereas in the country rock,
458 elongated patch of contact metamorphism minerals indicate an E-W stretching direction (Fig. 5).
459 Second, the main emplacement directions of the pegmatite dykes and quartz veins intrusive into the
460 Guérande granite indicate either NE–SW or E-W stretching direction depending on the area (Fig. 5). To
461 the northwest extremity, veins strike mostly NW–SE and their emplacement is compatible with the main
462 strike of the lineation recorded in the granite (i.e. N–S to NE–SW). In contrast, to the southwest, veins
463 strike mostly N-S and record an E–W stretching direction incompatible with the strike of the lineation in
464 the granite (i.e. N-S).

465 From the local occurrence of S/C fabrics and contact metamorphism indicators attesting for
466 potentially coeval N-S and E-W motions, we must consider the possibility that extension in the area
467 resulted in subhorizontal flattening strains, with local partitioning of dominant extension directions. At a
468 more regional scale, Gapais et al. (1993) showed that the extension direction was variable to the north
469 of the Guérande area, from E-W to N-S, according to the local orientation of the foliation, the stretching
470 lineations associated with the extension tending to show dominant dip-slip attitudes. Field evidences do
471 not support successive deformation events for these variable local kinematics. As a consequence, the
472 emplacement of pegmatite dykes and quartz veins, either from the southwest area which recorded E-W
473 stretching or from the northwest area which in contrast recorded NE-SW stretching, could be
474 synchronous and linked to the same deformation event.

475 It has been previously argued that extension in south Brittany was coeval with the dextral wrenching
476 along the South Armorican Shear Zone (Gumiaux et al., 2004). A combination of regional EW extension
477 and WNW-SSE strike-slip shearing might have contributed to the observed local scattering of extension
478 directions (Gapais et al., in press). Another additional working hypothesis could be a tendency of the
479 brittle upper crust to record chocolate-tablet type strains (Ramsay and Huber, 1983) induced by a
480 regional vertical shortening, which could constrain the partitioning of the kinematics in the underlying
481 ductile middle crust (Gapais et al. in press). Further arguments would require a detailed analysis of the
482 brittle strain patterns within the upper HP-LT units.

483 *9.2. Magmatism*

484 9.2.1. Source

485 As expected from the CL imaging (Fig. 13a), zircon grains from the sample GUE-3 yield a large range
486 of $^{207}\text{Pb}/^{206}\text{Pb}$ dates (Fig. 14a) suggesting the presence of heterogeneous inherited material. Because
487 most of the data are not concordant, it is impossible to discuss individual group of ages but basically two
488 main periods of inheritance can be seen with a few Late Archean-Proterozoic and numerous Paleozoic
489 cores (oldest and youngest $^{207}\text{Pb}/^{206}\text{Pb}$ dates of 2604 ± 18 Ma and 341 ± 27 Ma respectively). This spread
490 of ages is well known in the leucogranites from the Armorican Massif (see for example Tartèse et al.,
491 2011a).

492 The high peraluminous index (Fig. 8c and Table 3), the high I_{Sr} ratios and the low $\epsilon\text{Nd}(\text{T})$ values (Fig.
493 12) of the samples, together with the presence of inherited cores, with variable apparent ages, within
494 the dated zircon grains (Fig. 13 and Fig. 14a), and the old T_{DM} (Table 4), suggest a metasedimentary
495 source for the Guérande granite. The value of I_{Sr} and $\epsilon\text{Nd}(\text{T})$ plot at the transition between the fields
496 defined for the Brioverian and the Paleozoic sediments (Michard et al., 1985; Dabard et al., 1996; Fig.
497 12). This observation as well as the presence of inherited cores within the zircon grains with apparent
498 ages ranging from the Archean-Proterozoic to the Paleozoic suggest that both the Brioverian and the
499 Paleozoic sedimentary formations may have been involved in the partial melting event that produced
500 the Guérande granite.

501 Along a transect roughly perpendicular to the South Armorican Shear Zone, the Guérande granite
502 together with the others, mostly contemporaneous, syntectonic granites yield a peculiar evolution in
503 the I_{Sr} vs $\epsilon\text{Nd}(\text{T})$ diagram (Fig. 1 and Fig. 12). Indeed, from roughly north to south, the I_{Sr} values increase
504 while the $\epsilon\text{Nd}(\text{T})$ decrease from the Rostrenen (316 ± 3 Ma, U-Pb zircon; Euzen, 1993), Pontivy (344 ± 8
505 Ma, Rb-Sr whole-rock isochron; Bernard-Griffiths et al., 1985; 311 ± 2 Ma, $^{40}\text{Ar}/^{39}\text{Ar}$ muscovite; Cosca et
506 al., 2011), Lizio (316 ± 6 Ma, U-Pb zircon; Tartèse et al., 2011a), Questembert (316 ± 3 Ma, U-Pb zircon;
507 Tartèse et al., 2011b) to the Guérande granite (309.7 ± 1.3 Ma, U-Pb zircon and monazite; this study, see
508 part 9.4). We can propose three hypotheses at two different spatial scales to account for this trend:

509 (1) The Lizio, Questembert and Guérande granites have a pure metasedimentary source (Fig. 12).

510 Consequently, the N-S trend displayed by these three granites in Figure 12 could be explained by

511 a mixing between two metasedimentary end-members. To the north, the source of the
512 peraluminous granites is almost exclusively constituted by the Brioverian sediments whereas,
513 going south, the proportion of Paleozoic sediments, characterized by older model ages,
514 increases. This would be consistent with the fact that, the further south the granites are located,
515 the further away they are from the Cadomian domain, i.e. from the source for the Brioverian
516 sediments (Dabard et al., 1996), that are well expressed in the northern part of the Armorican
517 Massif.

518 (2) Comparing the Rostrenen-Pontivy granites to the Lizio-Questembert-Guérande granites in
519 Figure 12, the $\epsilon\text{Nd}(T)$ and I_{Sr} values for some of the samples from the Rostrenen and Pontivy
520 granites suggest a mantle contribution (two points with positive $\epsilon\text{Nd}(T)$ values). This hypothesis
521 is supported by the fact that granitoids with a mantle affinity have been described in the
522 Rostrenen massif (Plélauff monzodiorite; Euzen, 1993). We could tentatively link the mantle
523 contribution in the Rostrenen and Pontivy granites to the thickness of the continental crust,
524 which decreased from south to north at the end of the Carboniferous in Southern Brittany: the
525 crust was very thick below the Guérande and the Questembert massifs because these granites
526 were emplaced close to the core of the Hercynian belt whereas the crust was thinner below the
527 Lizio-Pontivy granites and almost not thickened at all below the Rostrenen massif (Ballèvre et
528 al., 2009). To the south of the South Armorican Shear Zone, the important thickness of the crust
529 could have prevented a mantle-derived underplated magma to reach the upper crustal level,
530 whereas such a process might have been possible to the north.

531 (3) Another hypothesis to explain the low I_{Sr} and the high $\epsilon\text{Nd}(T)$ measured for the northernmost
532 granites (Peucat et al., 1988) could be the contribution of juvenile components from the St-
533 Georges-sur-Loire synclinorium, located a few tens of kilometers to the east of the Questembert
534 region, and interpreted by some authors as the trace of an early Devonian back-arc basin
535 (Ballèvre et al., 2009 and references therein).

536 These three hypotheses are not individually exclusive and could have all contributed to the
537 southward evolution of the granitic sources during the Carboniferous evolution of the Hercynian belt in
538 the region.

539

540 9.2.2. Differentiation process

541 In the Harker diagrams (Fig. 9), several major- and trace-elements display well defined correlations
542 with SiO₂. These chemical variations could reflect a number of processes such as the melting of
543 heterogeneous sources combined with variable entrainment of peritectic assemblages and accessory
544 minerals in the melt (Stevens et al., 2007; Clemens and Stevens, 2012), a variable degree of partial
545 melting, wall-rock assimilation, a variation in the amount of mineral-melt segregation during
546 differentiation (Tartèse and Boulvais, 2010; Yamato et al., 2012) or a coalescence of several magma
547 batches issued from different sources followed by differentiation of these melts (Deniel et al., 1987; Le
548 Fort et al., 1987). For the Guérande granite, we believe that a process of fractional crystallization
549 implying the segregation of feldspar and biotite, hosting most accessory minerals, is the main process
550 behind the observed chemical variations. First, despite the fact that we cannot exclude source
551 heterogeneities, the similar εNd and the limited variation of I_{Sr} for the analyzed samples (Fig. 12) suggest
552 a derivation from a relatively homogeneous melt. Second, the low SiO₂ samples from the Guérande
553 granite display geochemical characteristics comparable to that of the liquids produced during
554 experimental melting of metasediments (Vielzeuf and Holloway, 1988; Patiño Douce and Johnston,
555 1991; Montel and Vielzeuf, 1997), with low content of ferromagnesian and CaO (Fe₂O₃+MgO+TiO₂ < 2%;
556 CaO < 1%), suggesting that they are close to anatectic melts (Patiño Douce, 1999) and that the amount
557 of peritectic or restitic minerals entrained from the source is negligible. Moreover, the K₂O content of
558 the Guérande samples is correlated with the sum Fe₂O₃+MgO+TiO₂, as both parameters decrease with
559 SiO₂ (Fig. 9), which is the opposite behavior expected for a process of entrainment of peritectic garnets
560 (Stevens et al., 2007; Clemens and Stevens, 2012). Third, two main observations based on trace-
561 elements behavior are in favor of a fractional crystallization process:

562 (1) The Ba and Sr contents, two elements compatible in biotite and feldspar, decrease largely with
563 increasing SiO₂ (Fig. 9a). Such variations in compatible elements (212 to 75 ppm for Sr and 411
564 to 133 ppm for Ba from GUE-15 to GUE-1) are very difficult to explain with a simple partial
565 melting process. In fact, by modeling the process of “partial or batch melting” (details in
566 Janoušek et al., 1997) using $D(\text{Sr})^{\text{res/liq}} = 4.4$ for a pure plagioclase and $D(\text{Ba})^{\text{res/liq}} = 6.36$ for a pure
567 biotite, the measured contents in Ba and Sr could be matched by a variation of the degree of
568 partial melting from about 0 to 80%, which is an unrealistic large range. On the other hand, such
569 important variations in compatible elements can be easily explained by a fractional
570 crystallization process involving a few tenths of a percent of mineral fractionation (Hanson,
571 1978; see part 9.3.3.2. for quantitative details).

572 (2) In Figure 9b, the excellent correlation between Zr and La reveals a common process between
573 zircon (which hosts Zr) and monazite (which hosts La), while the good correlation between Zr
574 and Fe₂O₃+Mgo+TiO₂, which both display the same overall range of variation (factor of 4
575 between 80 and 20ppm for Zr and factor 4 between 1.6 and 0.4 wt.% for Fe₂O₃+Mgo+TiO₂),
576 indicates that zircon and biotite shared a common magmatic history. In thin sections, zircon and
577 monazite occur mostly as inclusions within biotite, which suggests that the common magmatic
578 process which controls the distribution of Zr and La is the fractional crystallization of zircon- and
579 monazite-bearing biotite.

580

581 9.2.3. Fractional crystallization modeling

582 The inverse correlation between Fe₂O₃+MgO+TiO₂ and SiO₂ is consistent with the fractionation of
583 biotite and the depletions in CaO and K₂O for the SiO₂-rich samples are consistent with the fractionation
584 of plagioclase (CaO), potassic feldspar and biotite (K₂O) (Fig. 9). Here, we propose a quantification of the
585 amount of minerals that was segregated from the melt during the process of fractional crystallization,
586 first by using major elements and then by using trace-elements hosted by the main rock forming
587 minerals. The aplitic sample GUE-20 has been removed from these calculations because it displays a
588 much more evolved composition than the other samples, which is difficult to model solely by fractional

589 crystallization processes. Some of the characteristics of this sample may indeed be attributed to the
590 interaction with a fluid phase (discrete albitization as seen in the Q-P diagram (Fig. 8b) and enrichment
591 in Be (Table 3)).

592

593 *9.2.3.1. Major elements*

594 In Figures 15a and 15b, the whole-rock compositions of the unaltered samples from the Guérande
595 granite are plotted in Harker diagrams together with the theoretical composition of an An₂₀ plagioclase
596 and the average composition of biotite and potassic feldspar from the most primitive sample (GUE-4)
597 out of all the samples where chemical analyses of minerals have been carried out. In these diagrams, the
598 prolongation of the trends displayed by the granite samples allows to calculate the mineralogical
599 composition of the segregate assemblage (see Tartèse and Boulvais, 2010 for details about the
600 calculation), which yields an assemblage composed by 40-55 wt.% Kfs + 20-40 wt.% Bt + 5-40 wt.% An₂₀.

601 Independently, we used the “inverse major” plugin included in the GCD Kit software (Janoušek et al.,
602 2006) to calculate the amount and the mineralogical composition of the segregated cumulate required
603 to produce the chemical composition of the more evolved sample GUE-12 from the composition of the
604 less evolved sample GUE-15. The results obtained with this modeling (Table 5) are consistent with those
605 obtained with the first method and the differences between the calculated and the actual compositions
606 are small as indicated by a ΣR^2 (sum of the squared residuals) of 0.16. This modeling also implies that
607 apatite had a non-negligible contribution to the fractionating assemblage, as shown by the modal
608 composition of the calculated segregate assemblage that contains 45 wt.% Kfs + 21 wt.% Bt + 31 wt.%
609 An₂₀ + 4 wt.% Ap. Such amount of apatite is rather high but it allows for a good reproduction of the CaO
610 behavior. The P₂O₅ behavior is not well reproduced, as already noticed by Tartèse and Boulvais (2010),
611 and could perhaps be attributed to the mobility of P₂O₅ in deuteritic systems (Kontak et al., 1996). The
612 calculated amount of fractional crystallization in this model is 13 wt.%. These results are similar to those
613 obtained for the Lizio and Questembert granites by Tartèse and Boulvais (2010), who estimated that the
614 high SiO₂ samples from the Questembert granite could have derived from magmas similar to the low

615 SiO₂ samples of the Lizio granite if a fractionation of 16 wt.% of an assemblage composed of 51 wt.% Kfs
616 + 22 wt.% Bt + 27 wt.% Pl occurred.

617

618 9.2.3.2. *Trace-elements*

619 Ba is a compatible element in biotite and potassic feldspar whereas Sr is compatible in plagioclase
620 and apatite. In Figure 15c, the whole-rock compositions of the unaltered Guérande granite samples are
621 plotted in a Ba versus Sr diagram, with two theoretical models of evolution for the Ba and Sr contents
622 for a variable amount of fractional crystallization of the assemblage 0.45 Kfs + 0.21 Bt + 0.31 Pl + 0.04
623 Ap. The two models have been calculated using the Rayleigh distillation-type fractional crystallization for
624 two different ranges of Kd displayed in the table in Figure 15c. The two calculated trends reproduce the
625 trend defined by the Guérande granite samples and the calculated amount of crystallization between 10
626 and 30% is consistent with the previous amount of fractionate (13 wt.%) calculated using the major
627 elements. Sample GUE-2 displays higher degrees of mineral-melt segregation, but as noticed previously,
628 this sample underwent a weak albitization (Table 1). Therefore, its Sr and Ba contents could have been
629 modified during this hydrothermal process. Regarding other trace-elements whose behavior are
630 controlled by accessory minerals (Th, Zr, REE), an example of modeling developed by Tartèse and
631 Boulvais (2010) showed that even a minute fraction of mineral fractionation can account for the content
632 variations actually measured in the rocks. Such a modeling is not reproduced here and the interested
633 readers are invited to refer to these authors.

634 9.2.4. *Mechanism of differentiation*

635 The physical mechanism by which minerals segregated from the melt is still unclear. In fact, the
636 process of fractional crystallization is considered to be difficult to initiate in granitic magmas because of
637 the high viscosity of the melt and the low density contrast between crystals and melt (Yamato et al.,
638 2012). Tartèse and Boulvais (2010) proposed, on the basis of a petro – geochemical study of the Lizio
639 and Questembert granites (Fig. 1), that mineral-melt segregation could have occurred during magma
640 ascent in dykes and that, the largest amount of vertical motion the magma underwent, the most
641 evolved the magma becomes via differentiation. This hypothesis was tested by Yamato et al. (2012)

642 using numerical modeling, which showed that crystal segregation of rigid crystals from an ascending
643 magma is physically possible in a granitic melt, with typical density of 2400 kg.m^{-3} and viscosity of 10^4
644 Pa.s, as soon as (i) crystals involved are denser than the melt and (ii) the magma migration velocity, or
645 pressure gradient, within the dyke is low (see Fig.9 in Yamato et al., 2012).

646 In the Guérande granite, the most differentiated facies are overall located at the apical zone of the
647 intrusion (i.e. Ms-Turm coarse- to medium-grained granite, Fig. 2) suggesting that they originated from a
648 magma that travelled more distance than the magma involved in the root zone (i.e. Root facies : Ms – Bt
649 bearing, Fig. 2). As a consequence, the differentiation from the less to the more evolved samples of the
650 granite could have occurred when the magma was migrating toward the apical zone.

651 9.3. *Hydrothermal history*

652 Evidence for fluid-rock interaction in the Guérande granite includes:

653 (1) Numerous pegmatitic dykes and quartz veins crosscut the granite and recorded localized
654 magmato-hydrothermal activity.

655 (2) Greisens and albitized rocks have been described in the northwestern part of this intrusion (Fig.
656 2 and Fig. 8b). Greisenization generally occurs during the interaction with hot magmatic fluids
657 ($400\text{-}600^\circ\text{C}$; Jébrak and Marcoux, 2008) whereas albitization can be related to the interaction
658 with fluids of variable origins, either magmatic (Lee and Parsons, 1997) or post-magmatic
659 (Boulvais et al., 2007). Here, the facts that these albitized rocks are concentrated near the apical
660 zone of the intrusion and are spatially associated with greisenization, (i.e., a magmato-
661 hydrothermal process where albitization is complementary; Schwartz and Surjono, 1990),
662 suggest that both alterations resulted from the interaction with high temperature fluids at the
663 apex of the Guérande granitic body. Figure 8a allows to discriminate samples which have lost
664 their igneous compositions during such a hydrothermal alteration. Among them, the albitized
665 dyke samples GUE-19a and GUE-19b (Fig. 8b) display textural similarities with the aplitic dyke
666 GUE-20 (Table 1) suggesting that they share the same origin. This hypothesis is supported by the
667 fact that samples GUE-20, GUE-19a and 19b display similar REE patterns (Fig. 10). Also, these

668 three samples are enriched in Be, an independent feature related to the interaction with a fluid
669 phase.

670 (3) In Figure 11a, some samples (mostly the Ms-Turm bearing ones) display a strong increase in
671 their Cs and Sn contents, up to one order of magnitude, towards the apical zone of the granite
672 where cassiterite (SnO_2) occurs in quartz veins (Audren et al., 1975). In Figure 11b, Cs and Sn are
673 very well correlated; this trend could be interpreted as reflecting the magmatic behavior of Sn
674 and Cs, two highly incompatible elements, during fractional crystallization. Nevertheless, the
675 increase in the Cs content from 5 (GUE-17) to 77 ppm (GUE-1), for example, would imply an
676 unrealistic amount of fractional crystallization (more than 90 %) even if we consider that Cs
677 displays a purely incompatible behavior. The high Cs and Sn contents rather reflect an
678 enrichment in samples that interacted with fluids where Sn and Cs were strongly concentrated
679 (e.g., Förster et al., 1999).

680 (4) K/Rb values for the Guérande granite samples range from 243 down to 71, with values for the
681 Ms-Turm bearing samples always below 150. Such values below 150 are characteristic of the
682 pegmatite-hydrothermal evolution of Shaw (1968).

683 (5) The ratios between twin elements, such as Nb/Ta, may be fractionated during magmato-
684 hydrothermal processes either by muscovite and biotite fractionation (Stepanov et al., 2014) or
685 by fluid-rock interaction (Dostal and Chatterjee, 2000). Here, the Nb/Ta ratios decrease below a
686 value of 5 toward the apical zone (Fig. 11a) and is anti-correlated with Cs (Fig. 11b), likely
687 indicating that the decrease of the Nb/Ta ratios is the witness of the interaction with fluids, as
688 already noticed by Tartèse and Boulvais (2010) for the most evolved samples from the
689 Questembert granite.

690 (6) Chemical analyses of the muscovite grains (Fig. 7b) reveal that a secondary muscovitization
691 process occurred in the Guérande granite. This phenomenon increases from the Ms-Bt to the
692 Ms-Turm bearing samples and seems to be correlated with the decrease of the Nb/Ta ratios and
693 the increase of the Cs and Sn contents. These observations suggest that secondary
694 muscovitization could also be related to an interaction with fluids.

695 To sum up, the Guérande granite experienced both localized and pervasive magmato-hydrothermal
696 activity. Localized fluid circulation is recorded at the scale of the intrusion by the presence of numerous
697 quartz and pegmatitic veins whereas the pervasive hydrothermal interaction was prevalent at the apical
698 zone of the pluton.

699

700 *9.4. Timing of events*

701 U-Th-Pb dating of zircon and monazite from two samples from the Ms-Bt coarse- to medium-grained
702 granite (Fig. 14a and Fig. 14b) yielded dates equivalent within error (309 ± 2.6 Ma: Zrn GUE-3; $309.3 \pm$
703 6.1 Ma: Zrn GUE-8; 309.4 ± 1.9 Ma: Mnz GUE-3) and the analyses of the monazite grains from a sample
704 from the Ms–Bt fine-grained facies (GUE-4) yielded a Th-Pb date of 309.7 ± 1.3 Ma (Fig. 14c). Both zircon
705 and monazite ages are identical within error and are consistent with the field observation of Ouddou
706 (1984) that revealed mingling features at the contact between these two facies attesting for their
707 synchronous emplacement. We therefore conclude that the Guérande granite was emplaced ca. 310 Ma
708 ago. The muscovite Ar-Ar age of 307 ± 0.3 Ma, obtained by Le Hébel, 2002 for the undeformed granite,
709 could therefore be interpreted as a cooling age.

710 U-Th-Pb analysis of monazite and zircon grains from the dyke sample GUE-5 (Fig. 14d) yielded dates
711 equivalent within error (Zrn: 299.6 ± 5.4 Ma; Mnz: 302.5 ± 1.6 Ma), so this dyke was emplaced ca. 303
712 Ma ago, which is indicative of a second magmatic event in the vicinity. This age is directly comparable to
713 the muscovite Ar-Ar ages of 303.3 ± 0.5 Ma obtained for a quartz vein and of 303.6 ± 0.5 Ma and $304 \pm$
714 0.5 Ma obtained on a sheared granite and on a mylonitic granite, respectively (Le Hébel, 2002).

715 To summarize, considering that the Guérande granite displays S/C and mylonitic structures, it is
716 likely that the main phase of granite emplacement occurred syntectonically at ca. 310 Ma. Late
717 magmatic activity at ca. 303 Ma was still coeval with deformation. The circulation of fluids responsible
718 for the quartz veins emplacement and possibly for the secondary muscovitization process that
719 pervasively affected the apical zone of the Guérande granite (Fig. 7) likely occurred during both stages. If
720 large amounts of exsolved fluids are expected during the main emplacement stage of the Guérande

721 granite at ca. 310 Ma, the Ar-Ar age on muscovite grains from a quartz vein shows that hydrothermal
722 circulation was still active at ca. 303 Ma.

723 **10. Conclusion**

724 This study provides new constraints on the tectonic and magmatic history of the Guérande
725 peraluminous leucogranite and allows to shed some light on the mobility of elements during
726 hydrothermal activity. These new structural and petro-geochemical data lead to the following
727 conclusions:

728 (1) Structural and petrographic observations throughout the intrusion indicate that the
729 southwestern part of the Guérande granite represents the feeding zone whereas its
730 northwestern part corresponds to the apical zone.

731 (2) The Guérande granite was emplaced in an extensional tectonic regime and probably underwent
732 a partitioning of the deformation during its cooling. Indeed, the strike of quartz veins and
733 pegmatitic dykes and the lineations directions measured within the massif suggest that both N-S
734 and E-W stretching occurred synchronously in this area.

735 (3) Sr and Nd isotope data suggest that the Guérande granite formed by partial melting of
736 metasedimentary formations. When compared to others syntectonic peraluminous granites
737 from both the central and southern part of the Armorican Massif, from north to south, the
738 increase of I_{Sr} and the decrease of ϵNd could be explained by sedimentary sources becoming
739 gradually dominated by Paleozoic sediments relative to Brioverian sediments, combined with a
740 mantle contribution limited to the central part of the Armorican Massif.

741 (4) The magmatic history of the Guérande granite is controlled by fractional crystallization where an
742 amount of ~15% of fractionation of an assemblage composed of Kfs + Pl + Bt (\pm Ap \pm Zrn \pm Mnz \pm
743 Fe-Ti oxide) can explain the chemical variations observed between the samples.

744 (5) The apex of the Guérande leucogranite experienced pervasive hydrothermal alteration which
745 induced an enrichment in incompatible elements such as Sn and Cs, secondary muscovitization
746 and the decrease of geochemical ratio such as K/Rb and Nb/Ta in the samples.

747 (6) U-Th-Pb dating on zircon and monazite reveal that the Guérande granite was emplaced $309.7 \pm$
748 1.3 Ma ago and that a late magmatic activity synchronous with a hydrothermal circulation
749 occurred ca. 303 Ma ago. The magmatic and fluid-rock interaction events documented here
750 likely provides some key information for the U and Sn mineralization geometrically associated
751 with the Guérande intrusion.

752

753 **Acknowledgements**

754 This study is based on the work carried out by C. Ballouard for his Master's degree and was
755 supported by the 2012 and 2013 NEEDS-CNRS (AREVA - CEA) grants to M. Poujol. Rémi Sarrazin helped
756 during field work. The authors want to thank D. Vilbert (Géosciences Rennes) and J. Langlade (IFREMER,
757 Brest) for their contributions during the radiogenic isotopes and the electron microprobe analyses
758 respectively. This paper benefited from comments from P. Barbey and an anonymous reviewer on an
759 earlier version of the manuscript and from D.B. Clarke and A. Patiño Douce on the present version.

760

761 **References**

- 762 Audren, C., Jegouzo, P., Barbaroux, L., Bouysse, P., 1975. La Roche-Bernard, 449. Bureau de Recherches
763 Géologiques et Minières.
- 764 Ballèvre, M., Bosse, V., Ducassou, C., Pitra, P., 2009. Palaeozoic history of the Armorican Massif: Models for the
765 tectonic evolution of the suture zones. *Comptes Rendus Geosciences* 341, 174–201.
- 766 Barbarin, B., 1999. A review of the relationships between granitoid types, their origins and their geodynamic
767 environments. *Lithos* 46, 605–626.
- 768 Bernard-Griffiths, J., Peucat, J.J., Sheppard, S., Vidal, P., 1985. Petrogenesis of Hercynian leucogranites from the
769 southern Armorican Massif: contribution of REE and isotopic (Sr, Nd, Pb and O) geochemical data to the
770 study of source rock characteristics and ages. *Earth and Planetary Science Letters* 74, 235–250.
- 771 Berthé, D., Choukroune, P., Jegouzo, P., 1979. Orthogneiss, mylonite and non coaxial deformation of granites: the
772 example of the South Armorican Shear Zone. *Journal of Structural Geology* 1, 31–42.
- 773 Bosse, V., Balleve, M., Vidal, O., 2002. Ductile Thrusting Recorded by the Garnet Isograd from Blueschist-Facies
774 Metapelites of the Ile de Groix, Armorican Massif, France. *Journal of Petrology* 43, 485–510.
- 775 Bosse, V., Féraud, G., Ballèvre, M., Peucat, J.-J., Corsini, M., 2005. Rb–Sr and $^{40}\text{Ar}/^{39}\text{Ar}$ ages in blueschists from the
776 Ile de Groix (Armorican Massif, France): Implications for closure mechanisms in isotopic systems.
777 *Chemical Geology* 220, 21–45.
- 778 Bossière, G., 1988. Evolutions chimico-minéralogiques du grenat et de la muscovite au voisinage de l'isograde
779 biotite-staurotide dans un métamorphisme prograde de type barrovien: un exemple en Vendée littorale
780 (Massif Armoricain). *Comptes Rendus de l'Académie des Sciences, Paris, série II*, 306, 135–140.
- 781 Bouchez, J., Guillet, P., Chevalier, F., 1981. Structures d'écoulement liées à la mise en place du granite de Guérande
782 (Loire-Atlantique, France). *Bulletin de la Société Géologique de France*, XXIII-4, 387–399.
- 783 Boulvais, P., Ruffet, G., Cornichet, J., Mermet, M., 2007. Cretaceous albitization and dequartzification of Hercynian
784 peraluminous granite in the Salvezines Massif (French Pyrénées). *Lithos* 93, 89–106.
- 785 Brown, M., Pressley, R.A., 1999. Crustal melting in nature: Prosecuting source processes. *Physics and Chemistry of*
786 *the Earth Part A-Solid Earth and Geodesy* 24, 305–316.

787 Burg, J.P., Van Den Driessche, J., Brun, J.P., 1994. Syn-to post thickening extension in the Variscan Belt of western
788 Europe: modes and structural consequences. *Géologie de la France* 3, 33–51.

789 Cagnard, F., Gapais, D., Brun, J.P., Gumiaux, C., Van den Driessche, J., 2004. Late pervasive crustal-scale extension
790 in the south Armorican Hercynian belt (Vendée, France). *Journal of Structural Geology* 26, 435–449.

791 Capdevila, R., Corretgé, G., Floor, P., 1973. Les granitoides Varisques de la Meseta Ibérique. *Bulletin de la Société
792 Géologique de France*, XV-3-4, 209-228.

793 Carignan, J., Hild, P., Mevelle, G., Morel, J., Yeghicheyan, D., 2001. Routine Analyses of Trace Elements in
794 Geological Samples using Flow Injection and Low Pressure On-Line Liquid Chromatography Coupled to
795 ICP-MS: A Study of Geochemical Reference Materials BR, DR-N, UB-N, AN-G and GH. *geostandards
796 newsletter* 25, 187–198.

797 Cathelineau, M., 1981. Les Gisements Uranifères de la Presqu'île Guerandaise (Sud Bretagne); Approche
798 Structurale et Metallogénique. *Mineralium Deposita* 16, 227–240.

799 Chantraine, J., Autran, A., Cavelier, C., 2003. Carte géologique de la France à l'échelle du millionième, 6ème édition.
800 Bureau de Recherches Géologiques et Minières.

801 Chappell, B.W., White, A.J.R., Wyborn, D., 1987. The Importance of Residual Source Material (Restite) in Granite
802 Petrogenesis. *Journal of Petrology* 28, 1111–1138.

803 Chen, Y., Clark, A.H., Farrar, E., Wasteneys, H.A.H.P., Hodgson, M.J., Bromley, A.V., 1993. Diachronous and
804 independent histories of plutonism and mineralization in the Cornubian Batholith, southwest England.
805 *Journal of the Geological Society* 150, 1183–1191.

806 Clemens, J.D., Stevens, G., 2012. What controls chemical variation in granitic magmas? *Lithos* 134–135, 317–329.

807 Cogné, J., 1966. Les grands cisaillement hercyniens dans le Massif Armoricain et les phénomènes de granitisation.
808 Etages tectoniques. Edition de la Braconière, 179-192.

809 Collins, W.J., Sawyer, E.W., 1996. Pervasive granitoid magma transfer through the lower–middle crust during non-
810 coaxial compressional deformation. *Journal of Metamorphic Geology* 14, 565–579.

811 Cosca, M., Stunitz, H., Bourgeix, A.L., Lee, J.P., 2011. $^{40}\text{Ar}/^{39}\text{Ar}$ loss in experimentally deformed muscovite and biotite
812 with implications for $^{40}\text{Ar}/^{39}\text{Ar}$ geochronology of naturally deformed rocks. *Geochimica et Cosmochimica
813 Acta* 75, 7759–7778.

814 Dabard, M.P., Loi, A., Peucat, J.J., 1996. Zircon typology combined with Sm-Nd whole-rock isotope analysis to study
815 Brioverian sediments from the Armorican Massif. *Sedimentary Geology* 101, 243–260.

816 Debon, F., Le Fort, P., 1988. A cationic classification of common plutonic rocks and their magmatic associations:
817 principles, method, applications. *Bulletin de Minéralogie*, vol. 111, n°5, 493-510.

818 Deniel, C., Vidal, P., Fernandez, A., Fort, P.L., Peucat, J.J., 1987. Isotopic study of the Manaslu granite (Himalaya,
819 Nepal): inferences on the age and source of Himalayan leucogranites. *Contribution to Mineralogy and
820 Petrology*. 96, 78–92.

821 D'lemos, R.S., Brown, M., Strachan, R.A., 1992. Granite magma generation, ascent and emplacement within a
822 transpressional orogen. *Journal of the Geological Society* 149, 487–490.

823 Dostal, J., Chatterjee, A.K., 1995. Origin of topaz-bearing and related peraluminous granites of the Late Devonian
824 Davis Lake pluton, Nova Scotia, Canada: crystal versus fluid fractionation. *Chemical Geology* 123, 67–88.

825 Dostal, J., Chatterjee, A.K., 2000. Contrasting behaviour of Nb/Ta and Zr/Hf ratios in a peraluminous granitic pluton
826 (Nova Scotia, Canada). *Chemical Geology* 163, 207–218.

827 Euzen, T., 1993. Pétrogenèse des granites de collision post-épaississement. Le cas des granites crustaux et
828 mantelliques du complexe de Pontivy-Rostrenen (Massif Armoricain, France). *Mémoires Géosciences
829 Rennes*, 51, 360p.

830 Evensen, N.M., Hamilton, P.J., O'Nions, R.K., 1978. Rare-earth abundances in chondritic meteorites. *Geochimica et
831 Cosmochimica Acta* 42, 1199–1212.

832 Förster, H.-J., Tischendorf, G., Trumbull, R.B., Gottesmann, B., 1999. Late-Collisional Granites in the Variscan.
833 Erzgebirge, Germany. *Journal of Petrology* 40, 1613–1645.

834 Gasquet, D., Bertrand, J.-M., Paquette, J.-L., Lehmann, J., Ratzov, G., Guedes, R.D.A., Tiepolo, M., Boullier, A.-M.,
835 Scaillet, S., Nomade, S., 2010. Miocene to Messinian deformation and hydrothermal activity in a pre-
836 Alpine basement massif of the French western Alps: new U-Th-Pb and argon ages from the Lauzière
837 massif. *Bulletin de la Société Géologique de France* 181, 227–241.

838 Gapais, D., 1989. Shear structures within deformed granites: Mechanical and thermal indicators. *Geology* 17,
839 1144–1147.

840 Gapais, D., Lagarde, J.L., Le Corre, C., Audren, C., Jegouzo P., Casas Sainz, A., Van Den Driessche, J., 1993. La zone
841 de cisaillement de Quiberon: témoin d'extension de la chaîne varisque en Bretagne méridionale au
842 Carbonifère. *Comptes Rendus de l'Académie des Sciences, Paris, série II*, 316, 1123-1129.

843 Gapais, D., Brun, J.P., Gumiaux, C., Cagnard, F., Ruffet, G., Le Carlier de Veslud, C. Extensional tectonics in the
844 Hercynian Armorican belt (France). An overview. *Bulletin de la Société Géologique de France – in press.*

845 Goujou, J.C., 1992. Analyse pétro-structurale dans un avant-pays métamorphique: influence du plutonisme tardi-
846 orogénique varisque sur l'encaissant épi à mésozonal de Vendée. Document du Bureau de Recherche
847 Géologique et Minière, 216.

848 Gumiaux, C., 2003. Modélisation du cisaillement hercynien de Bretagne Centrale: déformation crustale et
849 implications lithosphériques. Thèse, Université de Rennes 1, 266p.

850 Gumiaux, C., Gapais, D., Brun, J.P., Chantaine, J., Ruffet, G., 2004. Tectonic history of the Hercynian Armorican
851 Shear belt (Brittany, France). *Geodinamica Acta* 17, 289–307.

852 Hanson, G.N., 1978. The application of trace elements to the petrogenesis of igneous rocks of granitic composition.
853 *Earth and Planetary Science Letters* 38, 26–43.

854 Hassenforder, B., Cogné, J., Barbaroux, L., Ottman, F., Berthois, L., 1973. Saint-Nazaire, 479. Bureau de Recherches
855 Géologiques et Minières.

856 Hughes, C.J., 1973. Spilites, keratophyres, and the igneous spectrum. *Geological Magazine* 109, 513–527.

857 Hutton, D.H.W., 1988. Granite emplacement mechanisms and tectonic controls: inferences from deformation
858 studies. *Earth and Environmental Science Transactions of the Royal Society of Edinburgh* 79, 245–255.

859 Icenhower, J., London, D., 1995. An experimental study of element partitioning among biotite, muscovite, and
860 coexisting peraluminous silicic melt at 200 MPa (H₂O). *American Mineralogist* 80, 1229–1251.

861 Icenhower, J., London, D., 1996. Experimental partitioning of Rb, Cs, Sr, and Ba between alkali feldspar and
862 peraluminous melt. *American Mineralogist* 81, 719–734.

863 Jackson, N.J., Willis-Richards, J., Manning, D.A.C., Sams, M.S., 1989. Evolution of the Cornubian ore field,
864 Southwest England; Part II, Mineral deposits and ore-forming processes. *Economic Geology* 84, 1101–
865 1133.

866 Jackson, S.E., Pearson, N.J., Griffin, W.L., Belousova, E.A., 2004. The application of laser ablation-inductively
867 coupled plasma-mass spectrometry to in situ U–Pb zircon geochronology. *Chemical Geology* 211, 47–69.

868 Janoušek, V., Rogers, G., Bowes, D.R., Vaňková, V., 1997. Cryptic trace-element variation as an indicator of reverse
869 zoning in a granitic pluton: the Ricany granite, Czech Republic. *Journal of the Geological Society* 154, 807–
870 815.

871 Janoušek, V., Farrow, C.M., Erban, V., 2006. Interpretation of Whole-rock Geochemical Data in Igneous
872 Geochemistry: Introducing Geochemical Data Toolkit (GCDKit). *Journal of Petrology* 47, 1255–1259.

873 Jébrak, M., Marcoux, É., 2008. Géologie des Ressources Minérales. Ministère des ressources naturelles et de la
874 faune.

875 Jégouzo, P., 1980. The South Armorican Shear Zone. *Journal of the Structural Geology* 2, 39–47.

876 Jones, K.A., Brown, M., 1990. High-temperature “clockwise” P-T paths and melting in the development of regional
877 migmatites: an example from southern Brittany, France. *Journal of Metamorphic Geology* 8, 551–578.

878 Kontak, D.J., Martin, R.F., Richard, L., 1996. Patterns of phosphorus enrichment in alkali feldspar, South Mountain
879 Batholith, Nova Scotia, Canada. *European Journal of Mineralogy* 8, 805–824.

880 Kretz, R., 1983. Symbols for rock-forming minerals. *American Mineralogist* 68, 277–279.

881 Lagarde, J.L., Capdevila, R., Fourcade, S., 1992. Granites et collision continentale; l'exemple des granitoides
882 carbonifères dans la chaîne hercynienne ouest-européenne. *Bulletin de la Société Géologique de France*
883 163, 597–610.

884 Lameyre, J., 1980. Les magmas granitiques: leurs comportements, leurs associations et leurs sources. Mémoire
885 hors-série de la Société Géologique de France 10, 51–62.

886 La Roche, H., Sussi, J., Chauris, L., 1980. Les granites à deux micas hercyniens français. *Sciences de la Terre*, 24, 5-
887 121.

888 Lee, M.R., Parsons, I., 1997. Dislocation formation and albitization in alkali feldspars from the Shap Granite.
889 *American Mineralogist* 82, 557–570.

890 Le Fort P., Cuney M., Deniel C., France-Lanord C., Shepard S.M.F., Upreti B.N., Vidal P., 1987. Crustal generation of
891 the Himalayan leucogranites. *Tectonophysics*, 134, 39-57.

892 Le Hébel, F., 2002. Déformation continentale et histoire des fluides au cours d'un cycle subduction, exhumation,
893 extension. Exemple des porphyroïdes Sud-Armoricains. Thèse, Université de Rennes 1, 218p.

894 Le Hébel, F., Vidal, O., Kienast, J.-R., Gapais, D., 2002. Les Porphyroïdes de Bretagne méridionale : une unité de HP–
895 BT dans la chaîne hercynienne. *Comptes Rendus Geoscience* 334, 205–211.

896 Le Hébel, F., Fourcade, S., Boiron, M.-C., Cathelineau, M., Capdevila, R., Gapais, D., 2007. Fluid history during deep
897 burial and exhumation of oil-bearing volcanics, Hercynian Belt of southern Brittany, France. *American*
898 *Journal of Science* 307, 1096–1125.

899 Lemarchand, J., Boulvais, P., Gaboriau, M., Boiron, M.-C., Tartèse, R., Cokinos, M., Bonnet, S., Jégouzo, P., 2012.
900 Giant quartz vein formation and high-elevation meteoric fluid infiltration into the South Armorican Shear
901 Zone: geological, fluid inclusion and stable isotope evidence. *Journal of the Geological Society* 169, 17–27.

- 902 Liew, T.C., Hofmann, A.W., 1988. Precambrian crustal components, plutonic associations, plate environment of the
903 Hercynian Fold Belt of central Europe: Indications from a Nd and Sr isotopic study. *Contribution to*
904 *Mineralogy and Petrology* 98, 129–138.
- 905 Ludwig, K. R., 2001. Isoplot/Ex version 2.49. A geochronological toolkit for Microsoft Excel. Berkeley
906 Geochronology Center, Special Publication 1a , 1-55.
- 907 Michard, A., Gurriet, P., Soudant, M., Albarede, F., 1985. Nd isotopes in French Phanerozoic shales: external vs.
908 internal aspects of crustal evolution. *Geochimica et Cosmochimica Acta* 49, 601–610.
- 909 Miller, C.F., Stoddard, E.F., Bradfish, L.J., Dollase, W.A., 1981. Composition of plutonic muscovite; genetic
910 implications. *The Canadian Mineralogist* 19, 25–34.
- 911 Montel, J.-M., Vielzeuf, D., 1997. Partial melting of metagreywackes, Part II. Compositions of minerals and melts.
912 *Contribution to Mineralogy Petrology* 128, 176–196.
- 913 Nachit, H., Razafimahefa, N., J.M., S., Carron, J., 1985. Composition chimique des biotites et typologie magmatique
914 des granitoïdes. *Comptes Rendus de l'Académie des Sciences, Paris, série II*, 301, 813-818.
- 915 Ouddou, D., 1984. Le Massif de Guérande-Le Croisic (Loire-Atlantique): Caractérisation géochimique et
916 minéralogique de l'évolution magmatique. Comportement de l'uranium. Thèse, INPL-CREGU Nancy, 309p.
- 917 Paquette, J.L., Tiepolo, M., 2007. High resolution (5 μ m) U–Th–Pb isotope dating of monazite with excimer laser
918 ablation (ELA)-ICPMS. *Chemical Geology* 240, 222–237.
- 919 Patiño Douce, A.E., Johnston, A.D., 1991. Phase equilibria and melt productivity in the pelitic system: implications
920 for the origin of peraluminous granitoids and aluminous granulites. *Contribution to Mineralogy and*
921 *Petrology* 107, 202–218.
- 922 Patiño Douce, A.E., 1999. What do experiments tell us about the relative contributions of crust and mantle to the
923 origin of granitic magmas? *Geological Society of London, Special Publication* 168, 55–75.
- 924 Peucat, J., Charlot, R., Mifdal, A., J., C., Aufran, A., 1979. Définition géochronologique de la phase bretonne en
925 Bretagne centrale, étude Rb-Sr de granites en domaine Centre-Armoricain. *Bulletin du BRGM (2) I4* , 349-
926 356.
- 927 Peucat, J.J., Jegouzo, P., Vidal, P., Bernard-Griffiths, J., 1988. Continental crust formation seen through the Sr and
928 Nd isotope systematics of S-type granites in the Hercynian belt of western France. *Earth and Planetary*
929 *Science Letters* 88, 60–68.
- 930 Pitra, P., Boulvais, P., Antonoff, V., Diot, H., 2008. Wagnerite in a cordierite-gedrite gneiss: Witness of long-term
931 fluid-rock interaction in the continental crust (Ile d'Yeu, Armorican Massif, France). *American Mineralogist*
932 93, 315–326.
- 933 Proust, J., Guennoc, P., Thion, I., Menier, D., 2009. Carte géologique de la France à 1/250 000 de la marge
934 continentale : Lorient, Bretagne Sud. Bureau de Recherches Géologiques et Minières; Centre National de
935 La Recherche Scientifique.
- 936 Prowatke, S., Klemme, S., 2006. Trace element partitioning between apatite and silicate melts. *Geochimica et*
937 *Cosmochimica Acta* 70, 4513–4527.
- 938 Puziewicz, J., Johannes, W., 1988. Phase equilibria and compositions of Fe-Mg-Al minerals and melts in water-
939 saturated peraluminous granitic systems. *Contribution to Mineralogy and Petrology* 100, 156–168.
- 940 Ramsay, J. G., Huber, M. I., 1983. Strain analysis, The techniques of modern structural geology, Vol. 1. Strain
941 Analysis (London: Academic Press).
- 942 Ren, M., Parker, D.F., White, J.C., 2003. Partitioning of Sr, Ba, Rb, Y, and LREE between plagioclase and
943 peraluminous silicic magma. *American Mineralogist* 88, 1091–1103.
- 944 Schwartz, M.O., Surjono, 1990. Greisenization and albitization at the Tikus tin-tungsten deposit, Belitung,
945 Indonesia. *Economic Geology* 85, 691–713.
- 946 Searle, M.P., 1999. Emplacement of Himalayan leucogranites by magma injection along giant sill complexes:
947 examples from the Cho Oyu, Gyachung Kang and Everest leucogranites (Nepal Himalaya). *Journal of Asian*
948 *Earth Sciences* 17, 773–783.
- 949 Shand, S., 1943. Eruptive rocks. Their genesis, composition, classification, and their relations to ore-deposits.
950 Wiley, New York, 2, 444.
- 951 Shaw, D., 1968. A review of K-Rb fractionation trends by covariance analysis. *Geochimica et Cosmochimica Acta* 32,
952 573–601.
- 953 Słaby, E., Martin, H., 2008. Mafic and Felsic Magma Interaction in Granites: the Hercynian Karkonosze Pluton
954 (Sudetes, Bohemian Massif). *Journal of Petrology* 49, 353–391.
- 955 Stepanov, A., Mavrogenes, J.A., Meffre, S., Davidson, P., 2014. The key role of mica during igneous concentration
956 of tantalum. *Contribution to Mineralogy and Petrology* 167, 1–8.
- 957 Stevens, G., Villaros, A., Moyen, J.-F., 2007. Selective peritectic garnet entrainment as the origin of geochemical
958 diversity in S-type granites. *Geology* 35, 9–12.

959 Strong, D.F., Hanmer, S.K., 1981. The leucogranites of southern Brittany; origin by faulting, frictional heating, fluid
960 flux and fractional melting. *The Canadian Mineralogist* 19, 163–176.

961 Tartèse, R., Boulvais, P., 2010. Differentiation of peraluminous leucogranites “en route” to the surface. *Lithos* 114,
962 353–368.

963 Tartèse, R., Poujol, M., Ruffet, G., Boulvais, P., Yamato, P., Košler, J., 2011a. New U-Pb zircon and ⁴⁰Ar/³⁹Ar
964 muscovite age constraints on the emplacement of the Lizio syn-tectonic granite (Armorican Massif,
965 France). *Comptes Rendus Geoscience* 343, 443–453.

966 Tartèse, R., Ruffet, G., Poujol, M., Boulvais, P., Ireland, T.R., 2011b. Simultaneous resetting of the muscovite K-Ar
967 and monazite U-Pb geochronometers: a story of fluids. *Terra Nova* 23, 390–398.

968 Triboulet, C., Audren, C., 1988. Controls on P–T–t deformation path from amphibole zonation during progressive
969 metamorphism of basic rocks (estuary of the River Vilaine, South Brittany, France). *Journal of*
970 *Metamorphic Geology*, 6, 117–133.

971 Turrillot, P., Augier, R., Faure, M., 2009. The top-to-the-southeast Sarzeau shear zone and its place in the late-
972 orogenic extensional tectonics of southern Armorica. *Bulletin de la Société Géologique de France* 180,
973 247–261.

974 Ugidos, J.M., Recio, C., 1993. Origin of cordierite-bearing granites by assimilation in the Central Iberian Massif
975 (CIM), Spain. *Chemical Geology* 103, 27–43.

976 Valois, J., 1975. Les formations métamorphiques de Pénaran (presqu’île de Guérande, Loire Atlantique) et leur
977 minéralisation uranifère. Thèse 3e cycle, Nancy, 136p.

978 Vielzeuf, D., Holloway, J.R., 1988. Experimental determination of the fluid-absent melting relations in the pelitic
979 system. *Contribution to Mineralogy and Petrology* 98, 257–276.

980 Vignerresse, J., 1983. Enracinement des granites armoricains estimé d’après la gravimétrie. *Bulletin de la société*
981 *Géologique et minéralogique de Bretagne*, vol. (C), 15 (1), 1-15.

982 Watson, E.B., Green, T.H., 1981. Apatite/liquid partition coefficients for the rare earth elements and strontium.
983 *Earth and Planetary Science Letters* 56, 405–421.

984 Willis-Richards, J., Jackson, N.J., 1989. Evolution of the Cornubian ore field, Southwest England; Part I, Batholith
985 modeling and ore distribution. *Economic Geology* 84, 1078–1100.

986 Wiedenbeck, M., Allé, P., Corfu, F., Griffin, W. I., Meier, M., Oberli, F., Quadt, A.V., Roddick, J. c., Spiegel, W., 1995.
987 Three Natural Zircon Standards for U-Th-Pb, Lu-Hf, Trace Element and Ree Analyses. *Geostandards*
988 *Newsletter* 19, 1–23.

989 Yamato, P., Tartèse, R., Duretz, T., May, D.A., 2012. Numerical modelling of magma transport in dykes.
990 *Tectonophysics* 526–529, 97–109.

991 Table Caption

992 Table 1: GPS coordinates and simplified petrographic description of the Guérande granite samples.

993 Ms-Bt: Ms-Bt coarse- to medium-grained granite; Ms-Turm: Ms-Turm coarse- to medium-grained granite; Fine:

994 Ms-Bt fine-grained granite; Root: root facies; Ch: chloritization; Ab: albitization; G: greisenization.

995

996 Table 2: Operating conditions for the LA-ICP-MS equipment.

997

998 Table 3: Whole-rock chemical compositions of the Guérande granite samples.

999 Root: root facies; Ms-Bt: Ms-Bt coarse- to medium-grained granite; Ms-Turm: Ms-Turm coarse- to medium-grained

1000 granite; Fine: Ms-Bt fine-grained granite; LOI: Loss on ignition; A/NK: molar $\text{Al}_2\text{O}_3/(\text{Na}_2\text{O} + \text{K}_2\text{O})$; A/CNK: molar

1001 $\text{Al}_2\text{O}_3/(\text{CaO} + \text{Na}_2\text{O} + \text{K}_2\text{O})$; bdl: below detection limit.

1002

1003 Table 4: Rb-Sr and Sm-Nd whole-rock data for the Guérande granite. Rb concentrations have been obtained by

1004 ICP-MS, other concentrations by isotopic dilution.

1005 **Two stages T_{DM} calculated using the equation of Liew and Hofmann (1988) for an age of 310 Ma.*

1006

1007 Table 5: Result of fractional crystallization modeling between the less differentiated sample GUE-15 and more

1008 differentiated sample GUE-12.

1009

1010

1011

1012

1013

1014

1015

1016

1017

1018

1019

1020 Figure caption

1021

1022 Figure 1: Structural map of the southern part of the Armorican Massif showing the localization of the Guérande
1023 granite. Modified from Gapais et al. (1993), Gumiaux (2003), the 1/1000000 geological map of France (Chantraine
1024 et al., 2003) and the 1/250000 geological map of Lorient (Proust et al., 2009). NBSASZ: Northern Branch of the
1025 South Armorican Shear Zone; SBSASZ: Southern Branch of the South Armorican Shear Zone.

1026 Figure 2 : Geological map of the Guérande granite modified after the 1/50000 geological maps of La Roche Bernard
1027 (Audren et al., 1975) and St-Nazaire (Hassenforder et al., 1973). The different petrographic facies and the alteration
1028 types are reported. Sampling sites with sample numbers are also indicated. Structural data (foliation planes
1029 orientations and strikes of lineation) are from Bouchez et al. (1981) and our own observations. Mineral
1030 abbreviations are from Kretz (1983).

1031

1032 Figure 3: Simplified cross section of the Guérande granite. The localization of the cross section is on Figure 1.
1033 Modified after Bouchez et al. (1981).

1034

1035 Figure 4: Representative pictures from the southwestern part (a, c, d) and the northwestern part (b, e, f) of the
1036 Guérande granite. a) Ms-Bt bearing root facies (sample GUE-13). The roughly defined foliation (S) is marked by
1037 muscovite and biotite stretching. b) Ms-Turm coarse- to medium-grained granite (sample GUE-18). c) Typical
1038 outcrop of the root facies with granite marked by a roughly defined foliation (F Granite) and a zone of isotropic
1039 granite (I Granite). Both facies are crosscut by a pegmatite dyke. d) Root facies with a roughly defined foliation (S).
1040 e) Mylonitic S/C granite (sample GUE-9). f) Large quartz vein cross cutting Ms-Turm coarse- to medium-grained
1041 granite near the contact with the micaschists and metavolcanics.

1042

1043 Figure 5: a-b) Pictures of stretching lineation (SL) in the Guérande massif: d) N030° stretching lineation in the
1044 mylonitic S/C sample GUE-9, e) E-W stretching lineation marked by contact metamorphism minerals in the
1045 micaschists localized at the contact with the Guérande granite. Both pictures are localized on the map. c-d-e) Rose
1046 diagram displaying the strikes of pegmatites, aplite dykes and quartz veins of three strategic areas from the south-

1047 west to the north-west of the Guérande granite. The numbers inside the diagrams (horizontal and vertical axes)
1048 represent the amount of measured dykes displaying a range of strike. The light grey areas represent the main strike
1049 of lineation (most of the lineation data are from Bouchez et al., 1981). n: number of measured dykes.

1050

1051 Figure 6 : Thin section photomicrographs showing the different petrographic facies of the Guérande granite. a) Root
1052 facies (Bt>Ms), b) Ms-Bt coarse- to medium grained granite (Ms>Bt) and c) Ms-Turm coarse- to medium-grained
1053 with two generation of Ms (MsI: primary muscovite; MsII: secondary muscovite). Mineral abbreviation from Kretz
1054 (1983).

1055

1056 Figure 7: Chemical compositions of plagioclase and muscovite from the Guérande granite. a) Triangular
1057 classification of plagioclase. b) Ternary Ti-Na-Mg diagram for muscovite and chemical map of Mg distribution in
1058 muscovite for the Ms-Turm granite sample GUE-1 and the Ms-Bt granite dyke GUE-5. The primary and secondary
1059 fields of muscovite are from Miller et al. (1981). In figure the inset “cleavage” refers to small muscovite grains
1060 located within foliation planes.

1061

1062 Figure 8 : a) Chemical (after Hughes, 1973) and b) chemical-mineralogical (after Debon and Le Fort, 1988)
1063 diagrams for the Guérande granite samples. Samples GUE-19a, 19b and 21 show evidences of alteration. In
1064 diagram b), the crosses indicate the location of common igneous rock: **gr** = granite, **ad** = adamellite, **gd** =
1065 granodiorite, **to** = tonalite, **sq** = quartz syenite, **mzq** = quartz monzonite, **mzdq** = quartz monzodiorite, **s** = syenite,
1066 **mz** = monzonite, **mzgo** = monzogabbro. Q and P parameters are expressed in molar proportion multiplied by 1000.
1067 c) Shand (1943) diagram ($A/CNK = Al_2O_3/(CaO+Na_2O+K_2O)$; $A/NK = (Al_2O_3/(Na_2O+K_2O))$; molar proportions)
1068 where unaltered and altered samples are distinguished on the basis of figures a) and b). Lizio and Questembert
1069 granite samples are shown for comparison (Tartèse and Boulvais, 2010).

1070

1071 Figure 9 : Harker (a) and bivariate diagrams (b) of selected major- and trace-elements for the Guérande granite.

1072

1073 Figure 10: Chondrite normalized REE patterns of the Guérande granite samples. Normalization values from
1074 Evensen et al. (1978).

1075

1076 Figure 11 : a) Evolution of some geochemical tracers sensible to the interaction with fluids as a function of the
1077 distance to the NW edge of the Guérande granite. b) Evolution of chosen tracers as a function of the concentration
1078 of Cs.

1079

1080 Figure 12 : Sr and Nd isotopic compositions of the Guérande granite compared with the Lizio, Questembert (Tartèse
1081 and Boulvais, 2010), Pontivy and Rostrenen granite (Peucat et al., 1979 ; Euzen, 1993). ϵNd and I_{Sr} are calculated
1082 for an age of 310 Ma. The vertical bars representing $\epsilon\text{Nd(T)}$ composition of the Brioverian and Paleozoic sediments
1083 from Central Brittany are calculated from Michard et al. (1985) and Dabard et al. (1996). The exceptionally high
1084 $\epsilon\text{Nd(T)}$ value of 0.5 measured in the Paleozoic sediments (Michard et al., 1985) is not reported in the figure. The
1085 arrow in the figure represents north – south evolution of the isotopic compositions of the Carboniferous
1086 peraluminous granites of the Armorican Massif.

1087

1088 Figure 13 : selected images of zircon and monazite grains. a-b-d) cathodoluminescence images of zircons from the
1089 sample GUE-3, GUE-8 and GUE-5. c) Th chemical map of monazite from the sample GUE-4. Dashed circles
1090 represent the location of LA-ICP-MS analyses with the corresponding $^{206}\text{Pb}/^{238}\text{U}$ ages in Ma.

1091

1092 Figure 14 : a) Tera-Wasserburg diagram displaying the analyses made on zircon of the sample GUE-3. The Grey
1093 ellipses represent the inherited zircons and the dashed ellipses represent zircon submitted to a loss or a gain in
1094 common lead. #: $^{207}\text{Pb}/^{206}\text{Pb}$ ages at 1σ . b-c-d) $^{206}\text{Pb}/^{238}\text{U}$ vs $^{208}\text{Pb}/^{232}\text{Th}$ concordia diagram for monazite of the
1095 sample GUE-3, GUE-4 and GUE-5. The dashed ellipses represent the analyses not used for the calculation of
1096 Concordia ages. In the diagrams error ellipses are plotted at 1σ .

1097

1098 Figure 15 : a-b) Harker diagrams displaying the whole-rock compositions of the unaltered samples from the
1099 Guérande granite. The black stars represent the average compositions of potassic feldspar and biotite from the
1100 sample GUE-4 and the composition of a theoretical plagioclase (An₂₀). The grey areas represent the magmatic
1101 trends defined by the whole-rock data including the errors. The intersection of this trend with the assemblage

1102 Bt+An₂₀+Kfs encompasses the mineralogical composition of the segregate. c) Ba vs Sr diagram displaying the
1103 whole-rock compositions of the unaltered samples from the Guérande granite. The two lines represent two different
1104 models of evolution of Ba and Sr compositions in a liquid during the fractional crystallization of an assemblage
1105 made of 0.45Kfs+0.31Pl+0.21Bt+0.04Ap. The numbers under the line indicate the amount of the assemblage
1106 fractionated from the melt in Wt.%. The primitive composition of the liquid used to model fractional crystallization
1107 is the composition of sample GUE-15. Kd used and presented in the table in inset in the diagram are from a. Hanson,
1108 (1978); b. Icenhower and London, (1996); c. Ren et al., (2003); d. Icenhower and London, (1995); e. Watson and
1109 Green, (1981); f. Prowatke and Klemme, (2006).

Figure 1
[Click here to download high resolution image](#)

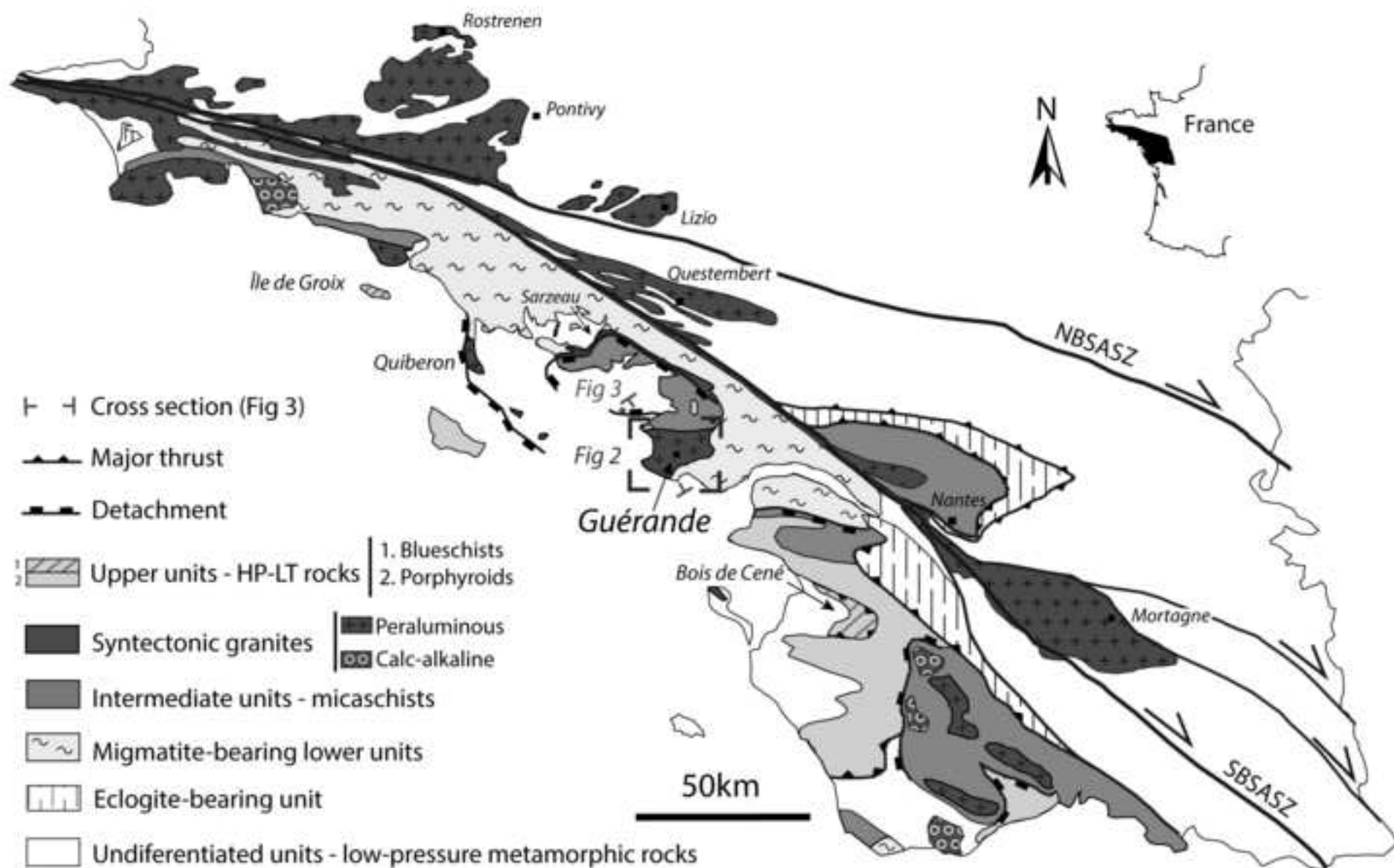


Figure 2
[Click here to download high resolution image](#)

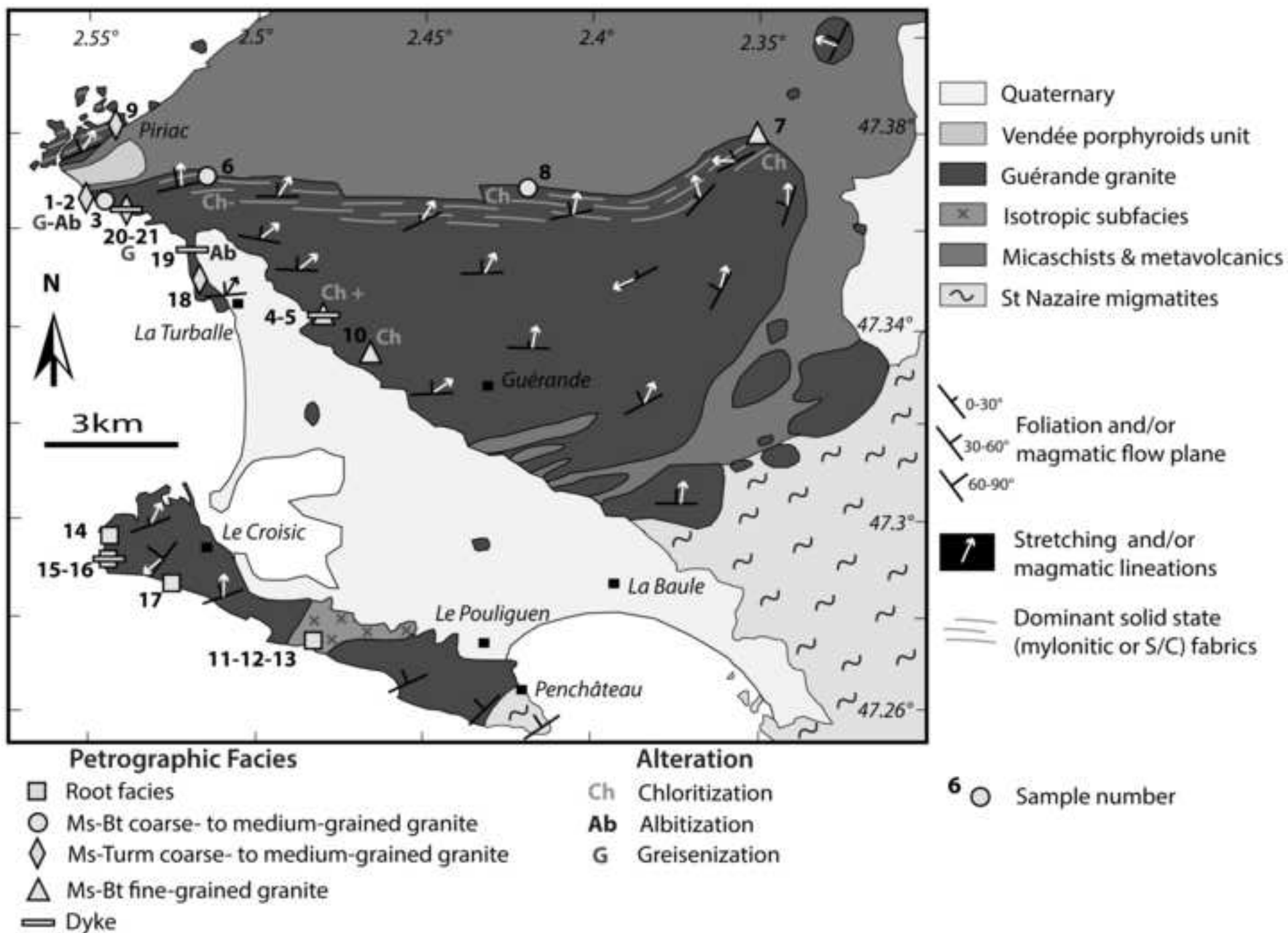


Figure 3
[Click here to download high resolution image](#)

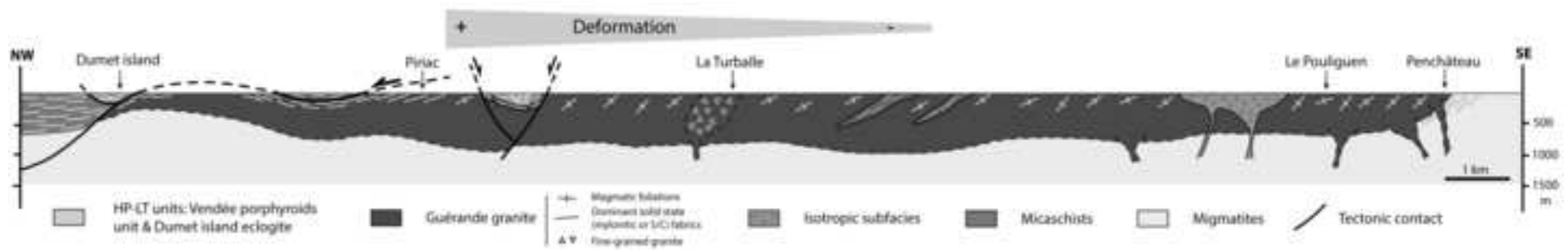


Figure 4
[Click here to download high resolution image](#)

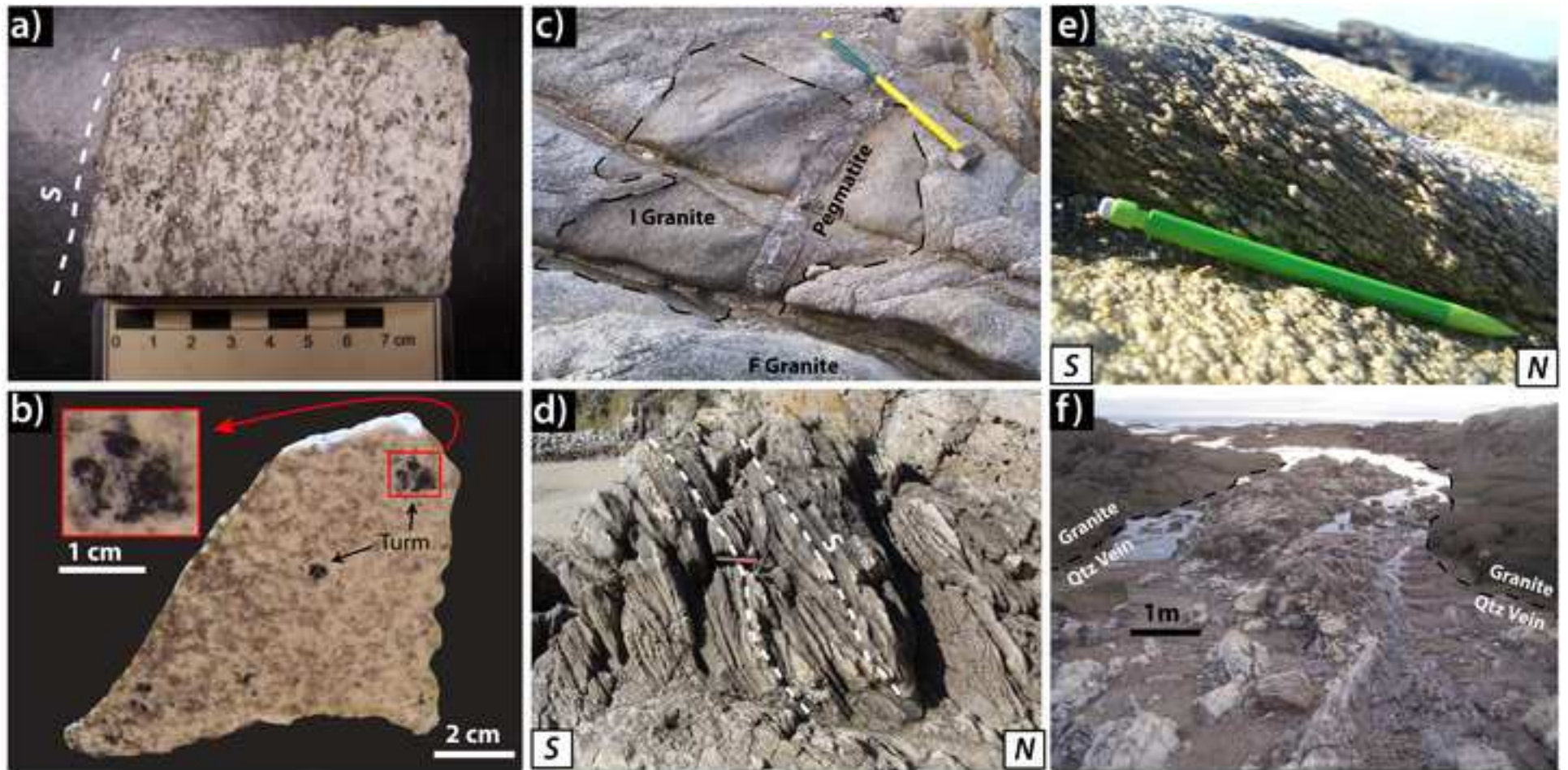


Figure 5
[Click here to download high resolution image](#)

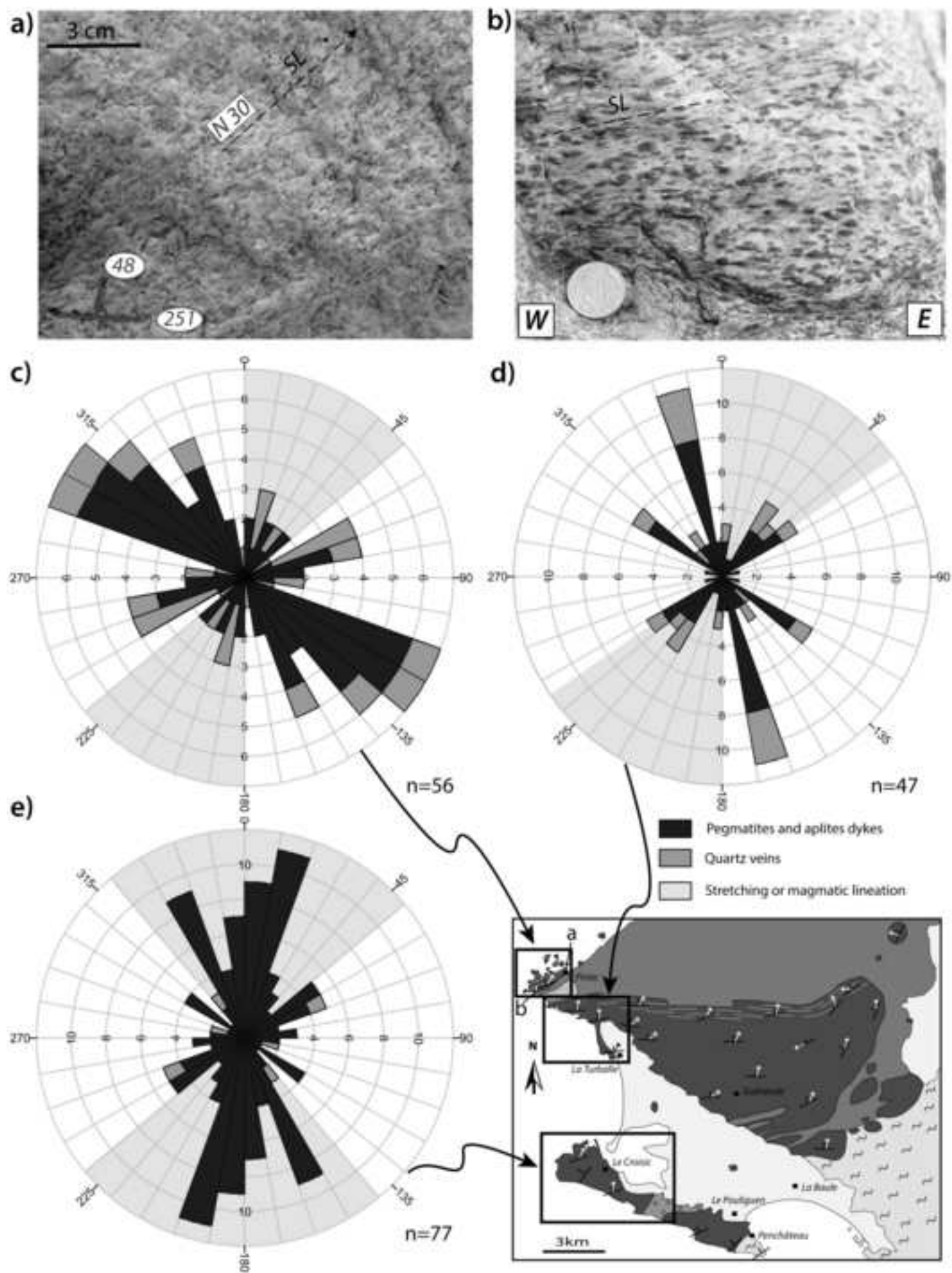


Figure 6
[Click here to download high resolution image](#)

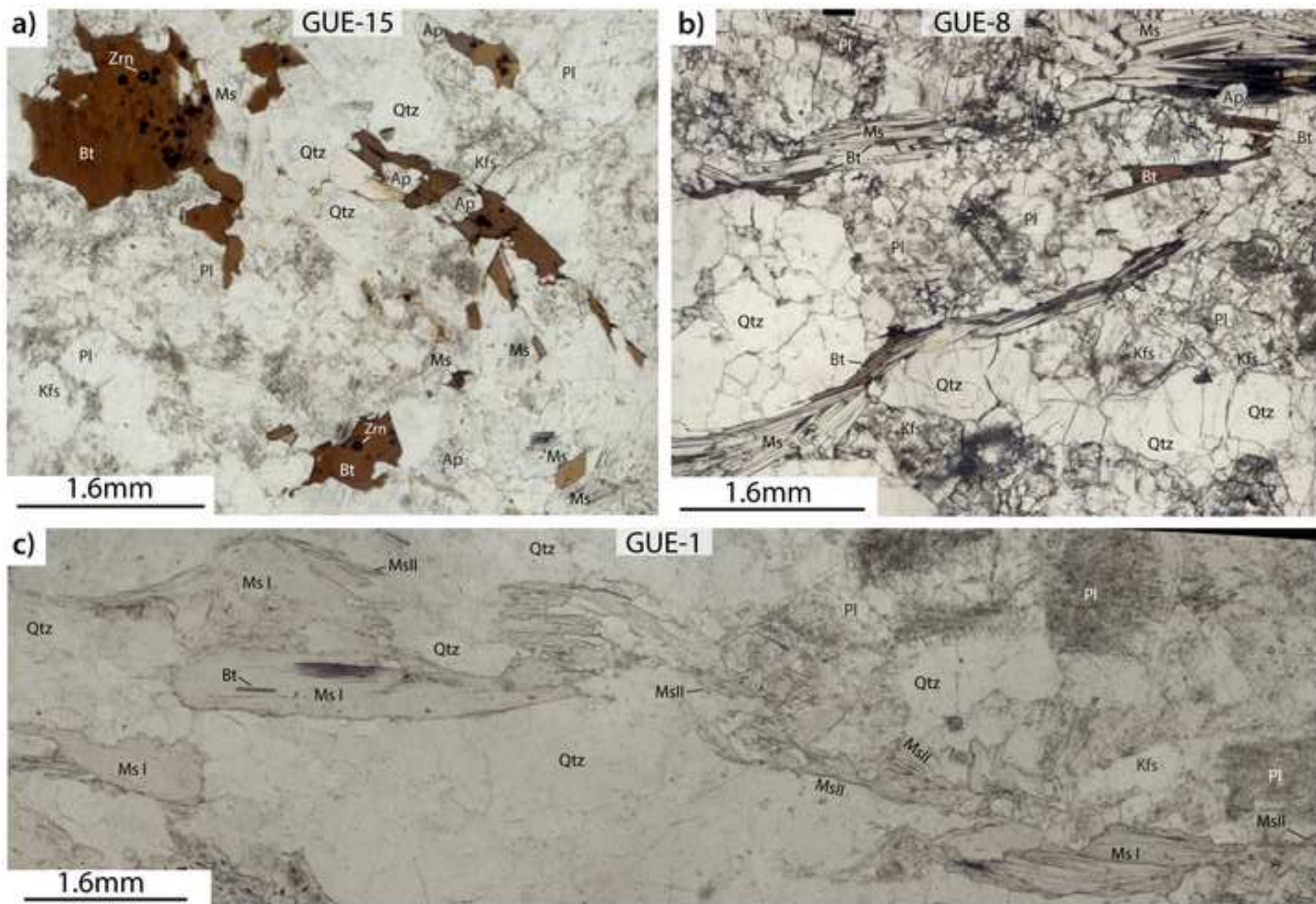


Figure 7
[Click here to download high resolution image](#)

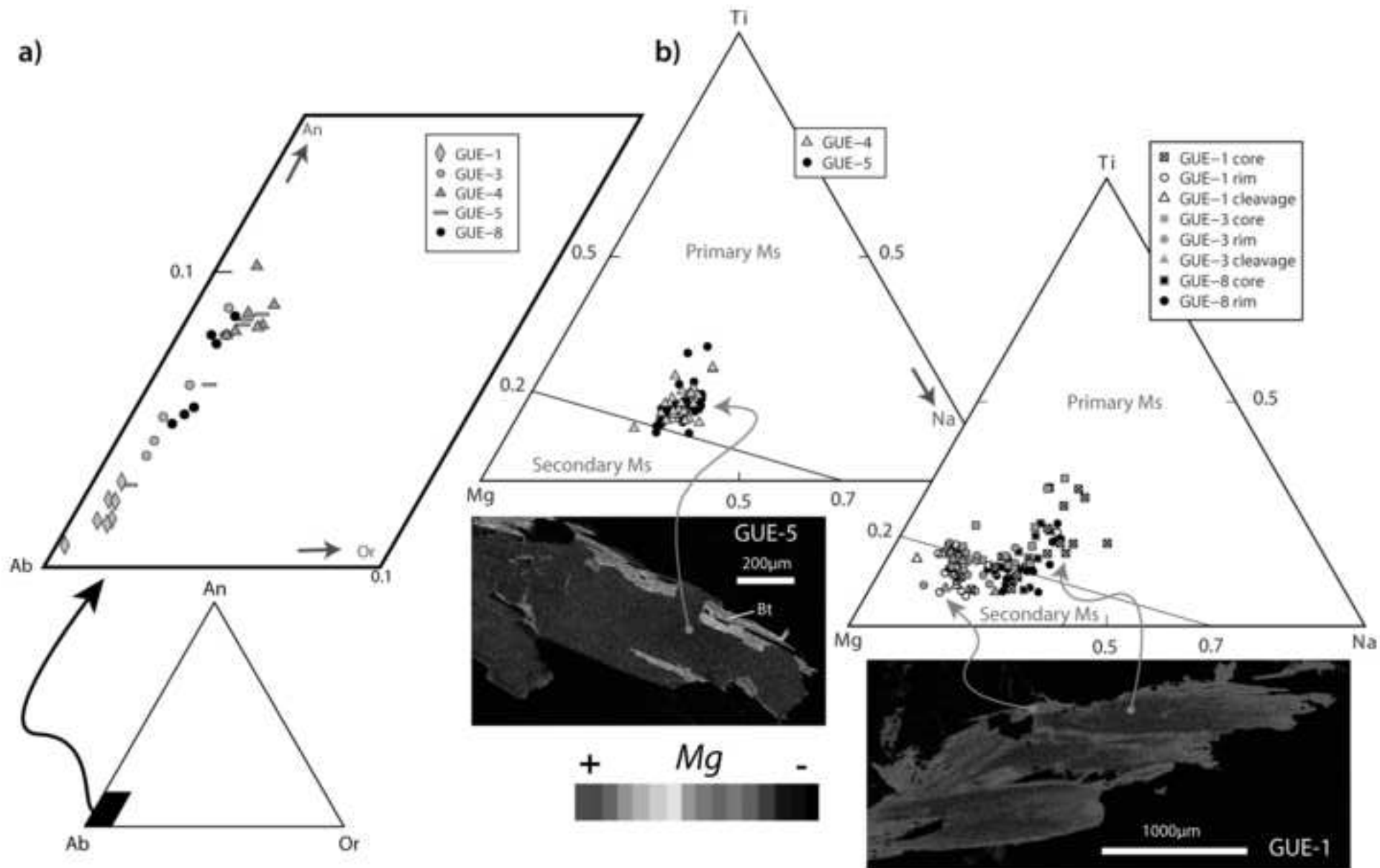


Figure 8
[Click here to download high resolution image](#)

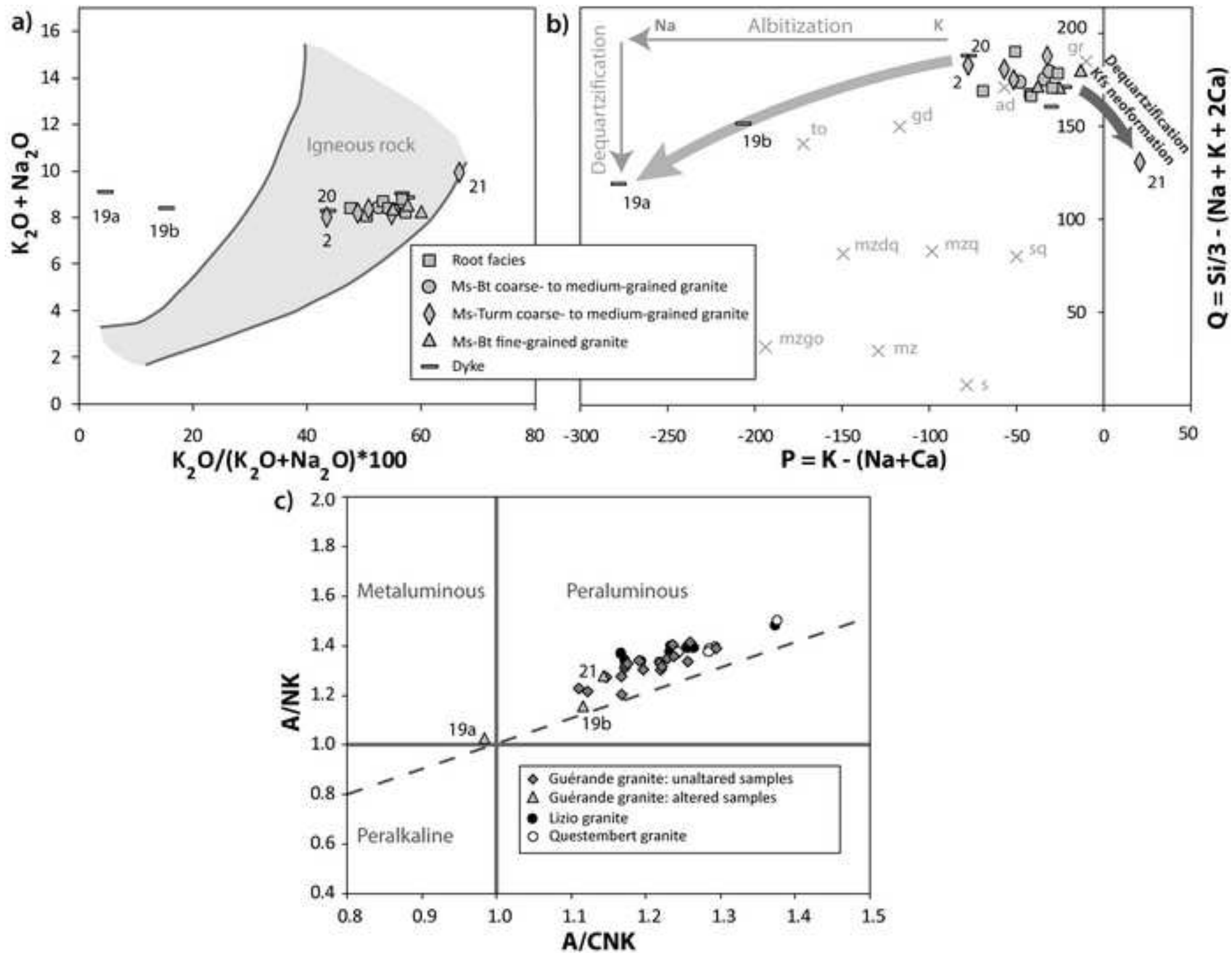


Figure 9
[Click here to download high resolution image](#)

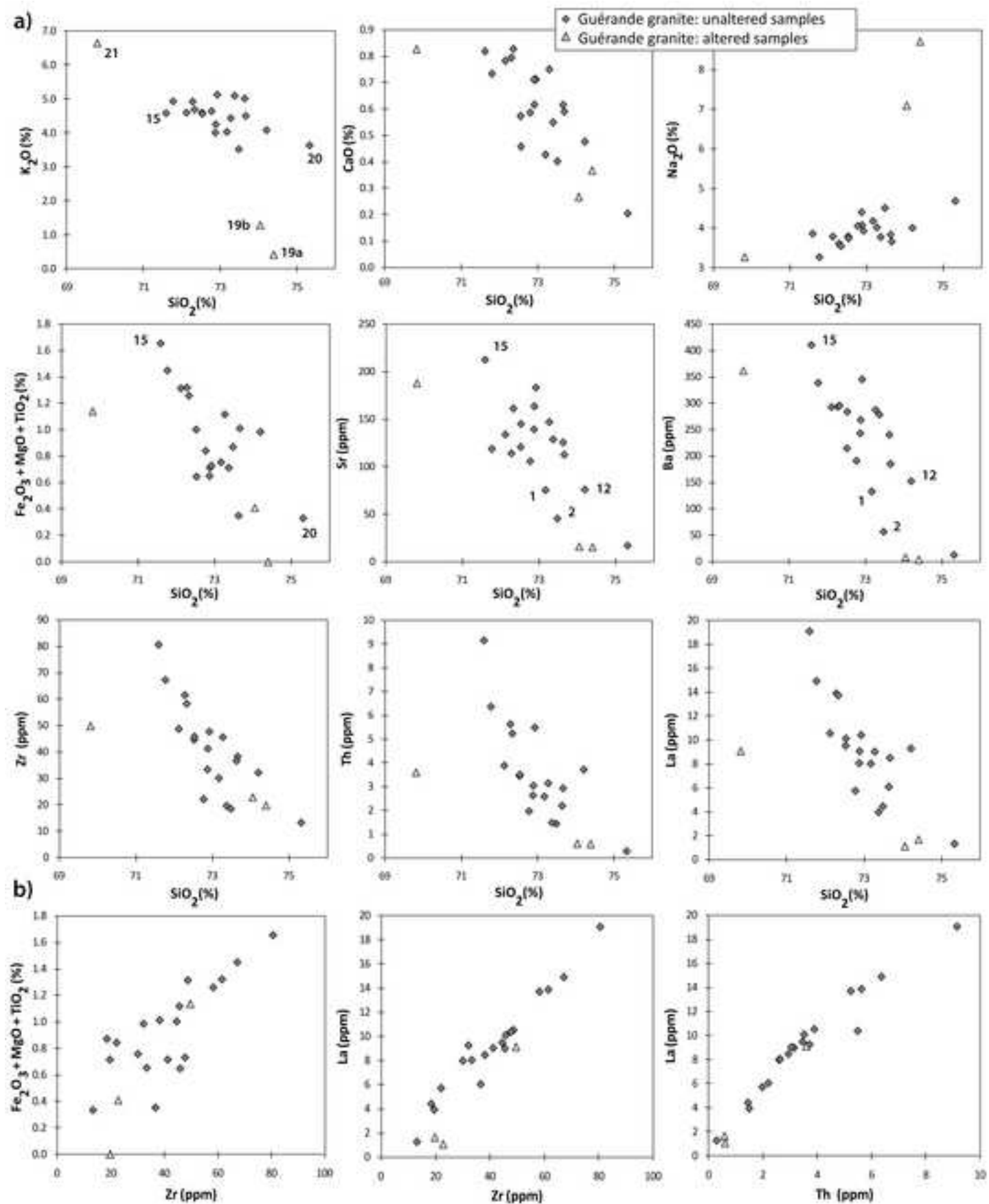


Figure 10
[Click here to download high resolution image](#)

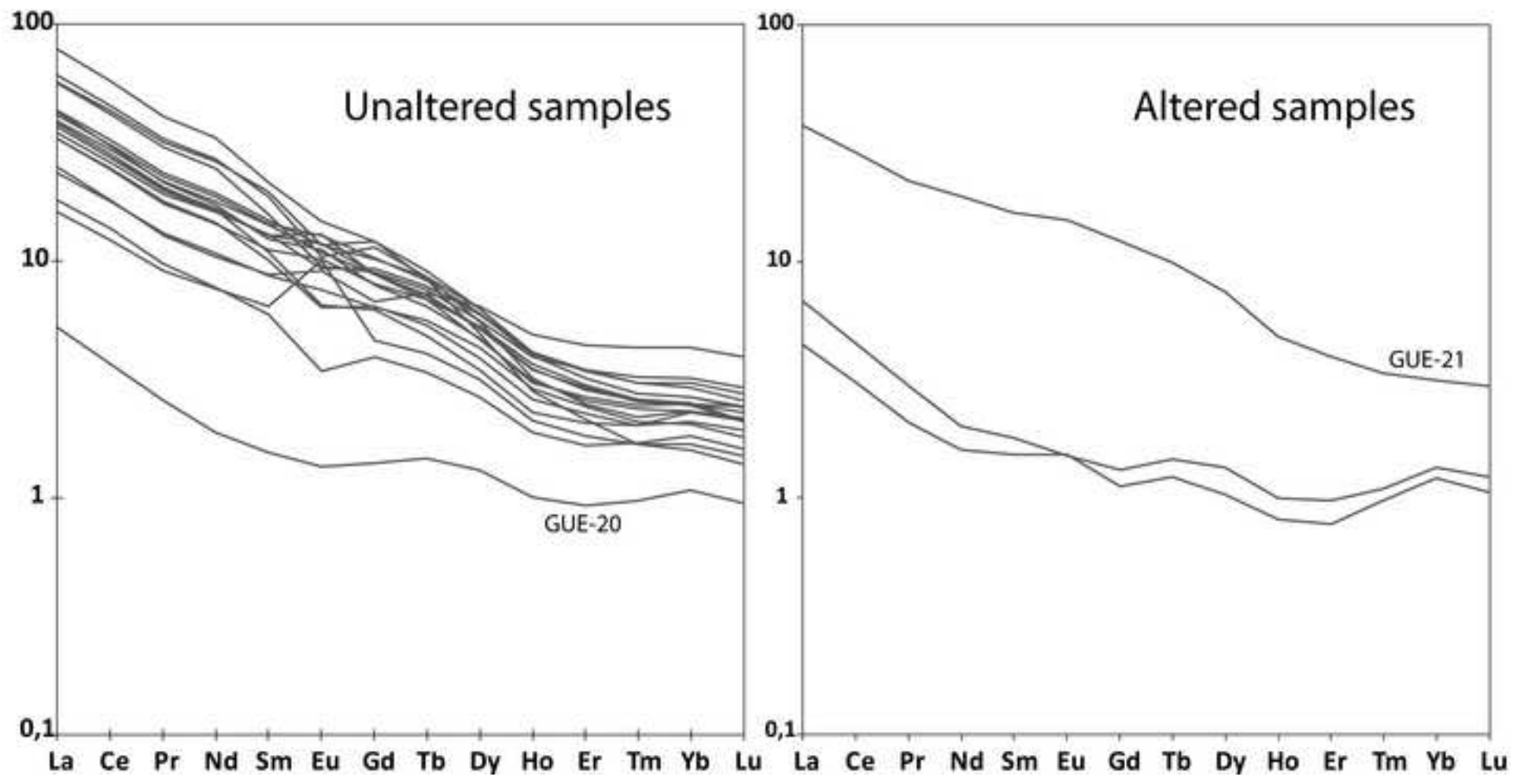


Figure 11
[Click here to download high resolution image](#)

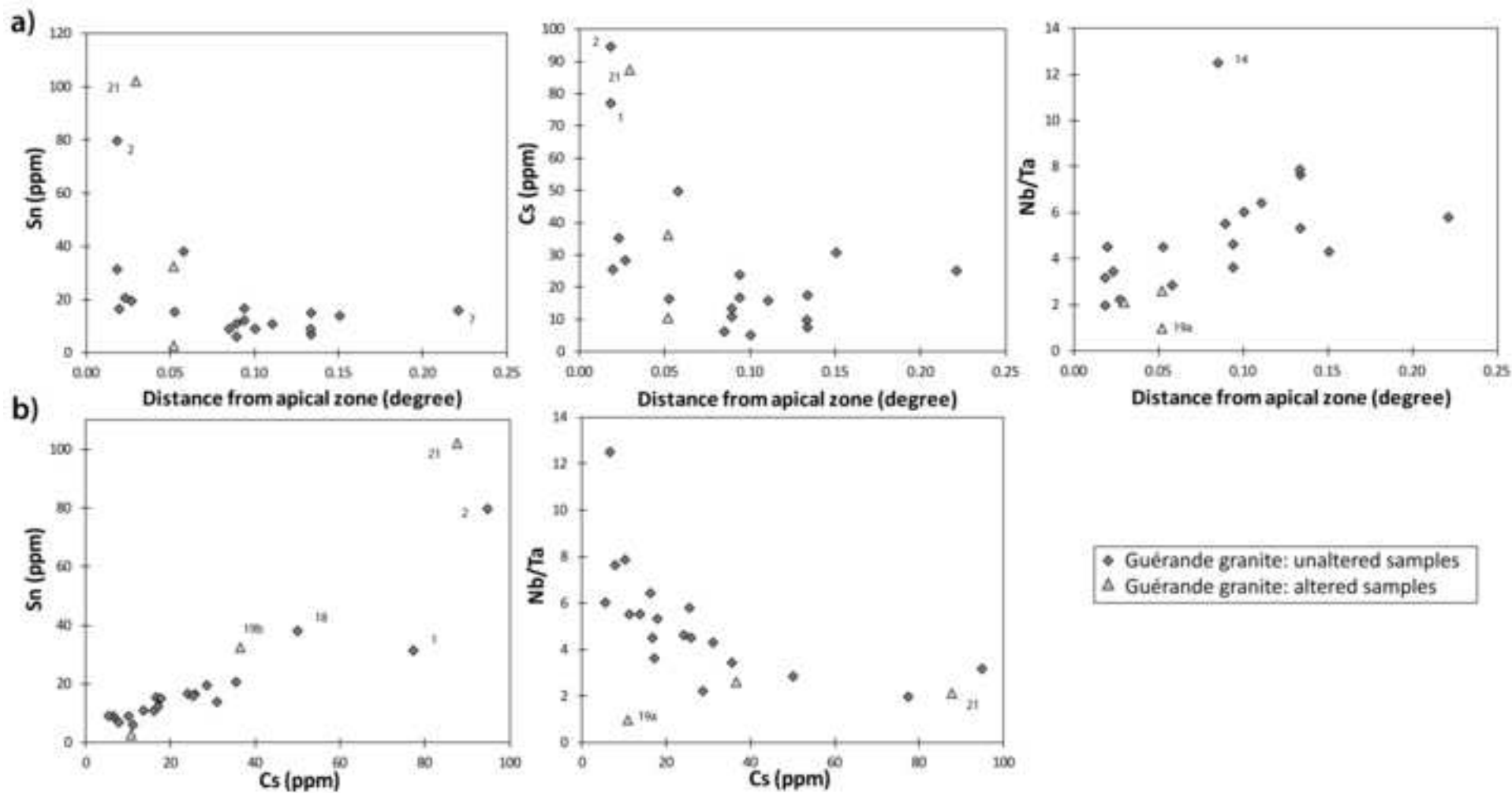


Figure 12
[Click here to download high resolution image](#)

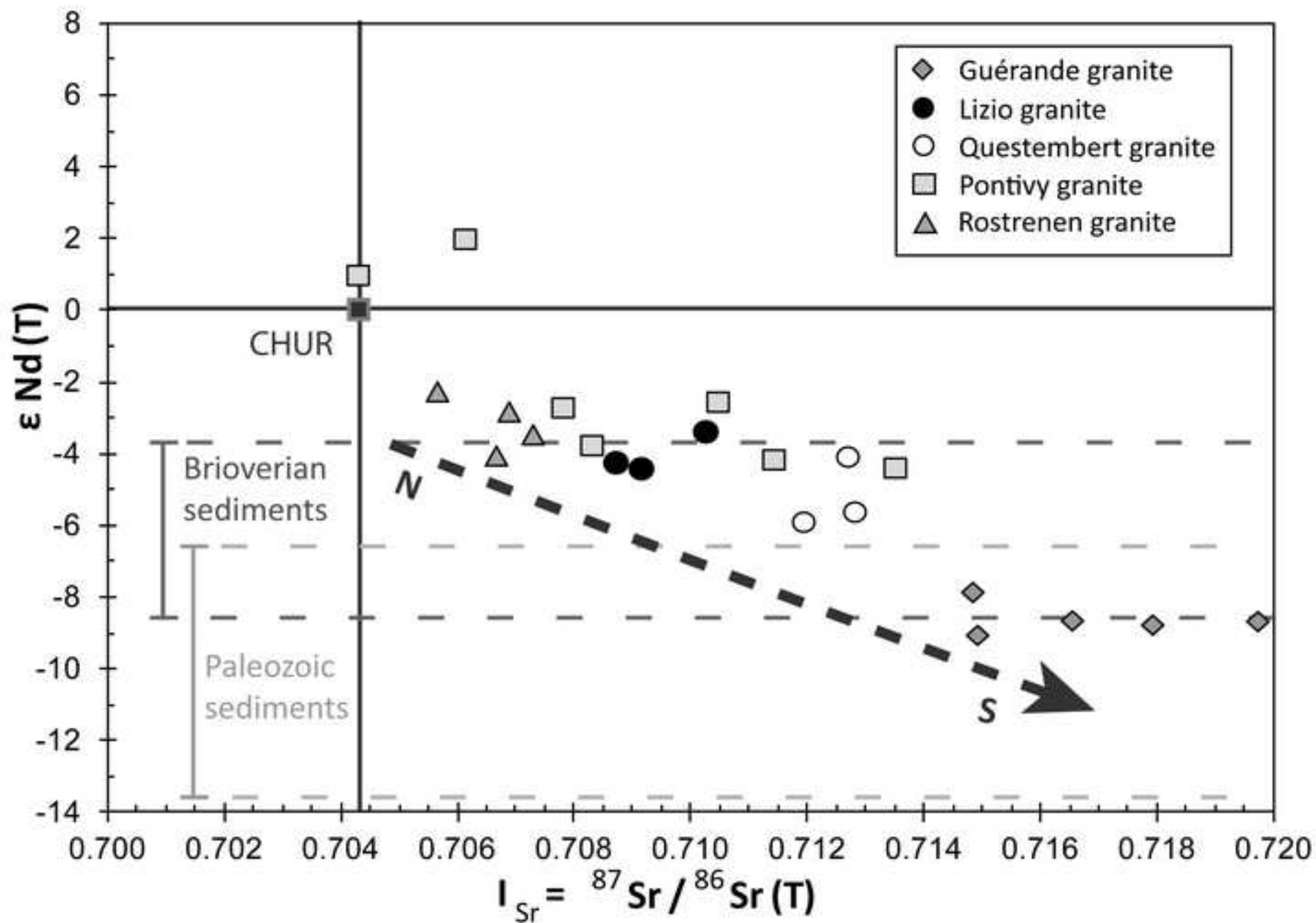


Figure 13
[Click here to download high resolution image](#)

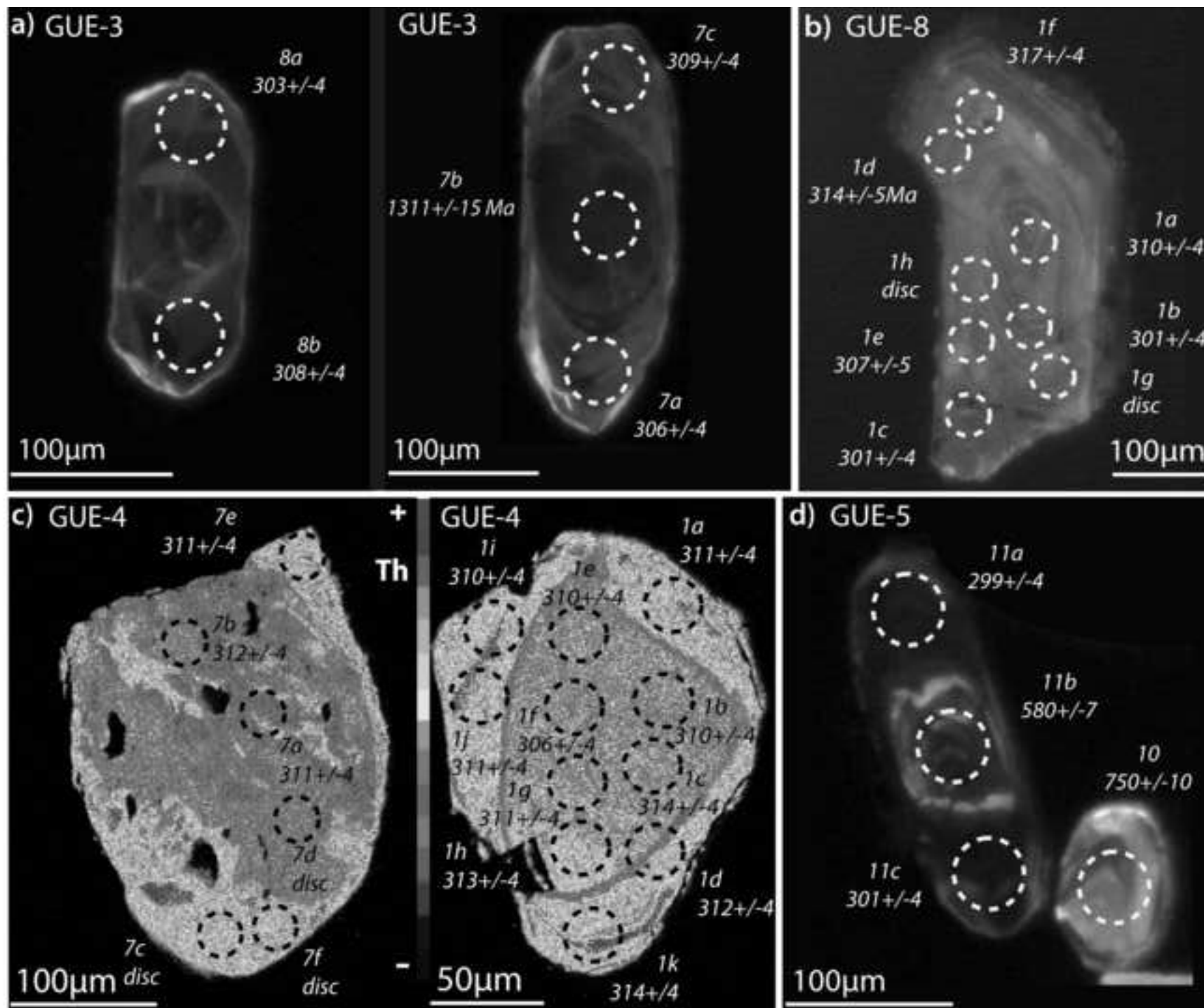


Figure 14

[Click here to download high resolution image](#)

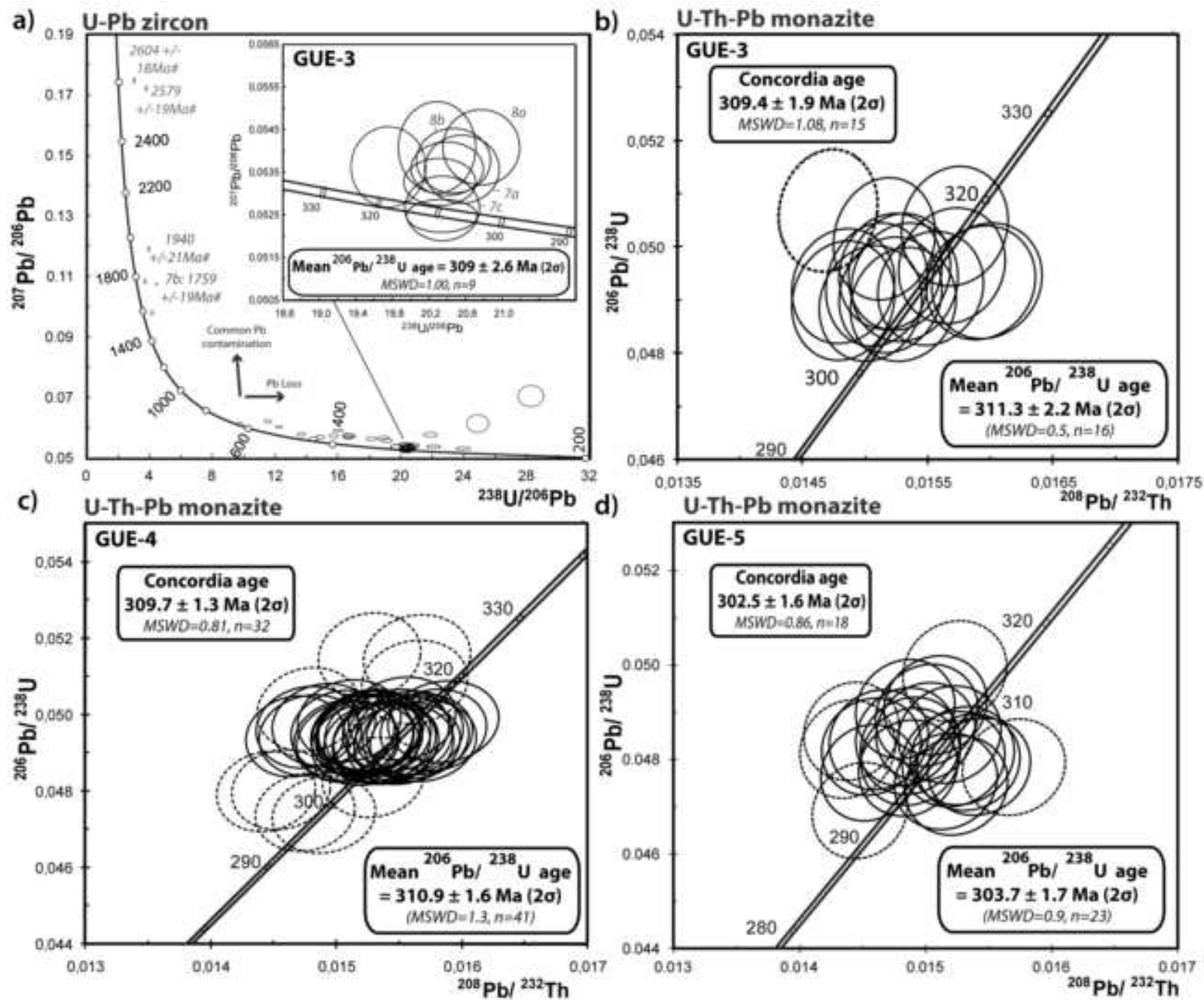


Figure 15

[Click here to download high resolution image](#)

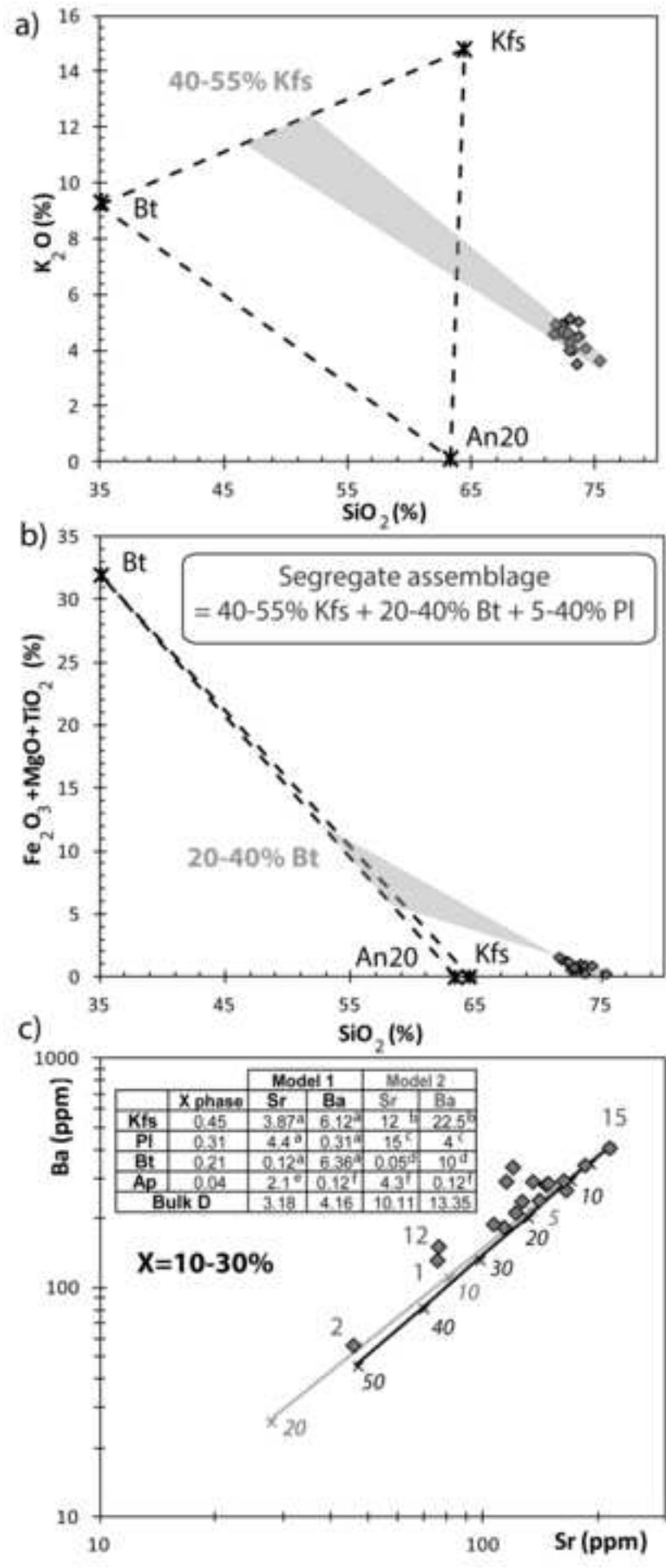


Table 1

[Click here to download Table: Table_1_Ballouardetal.docx](#)

Sample	Longitude (°)	Latitude (°)	Facies	Texture	Strain	Mineralogy	Alteration
GUE-11	-2.484200	47.274183	Root	Medium-grained (2mm), roughly defined foliation	+	Ms>>Bt	
GUE-12	-2.484200	47.274183	Root	Fine- to medium-grained (1-3mm), isotropic		Ms>Bt	
GUE-13	-2.484533	47.274367	Root	Medium-grained (2-3mm), roughly defined foliation	+	Ms>>Bt	
GUE-14	-2.546383	47.296217	Root	Fine-grained (1mm), isotropic		Ms>Bt	
GUE-15	-2.546417	47.291733	Root	Medium-grained (2-3mm), roughly defined foliation		Bt>Ms	
GUE-17	-2.526550	47.286967	Root	Fine-grained (1-2mm), solid state fabric	+	Ms>>Bt>Grt	
GUE-3	-2.547297	47.368122	Ms-Bt	Medium-to coarse grained (2-4mm), magmatic foliation	+	Ms>Bt	
GUE-6	-2.515918	47.370945	Ms-Bt	Medium- to fine-grained (1-3mm), S/C fabric	++	Ms>Bt	
GUE-8	-2.417652	47.368925	Ms-Bt	Coarse-grained (3-5mm), isotropic		Ms>Bt	Ch-
GUE-1	-2.552081	47.369195	Ms-Turm	Coarse-grained (3-5mm), magmatic foliation	+	Ms>>Turm> Bt	
GUE-2	-2.552081	47.369195	Ms-Turm	Coarse-grained (3-4mm), shear zone	++	Ms >> Turm	Ab-
GUE-9	-2.548596	47.381192	Ms-Turm	Fin- to medium-grained (<0.5-2mm) , S/C mylonite	+++	Ms>>Turm	
GUE-18	-2.517417	47.350167	Ms-Turm	Medium- to coarse-grained (2-3mm), isotropic		Ms>>Bt>Turm	
GUE-21	-2.541317	47.365750	Ms-Turm	Coarse-grained (3-5mm), magmatic foliation	+	Ms>>Turm	G?
GUE-4	-2.481191	47.342346	Fine	Fine-grained (0.5-2mm), isotropic		Ms>Bt	
GUE-7	-2.346883	47.380000	Fine	Fine-grained (0.5-2mm), solid state fabric	+	Ms>Bt	Ch
GUE-10	-2.466283	47.334767	Fine	Fine-grained (1-2mm), isotropic		Ms>Bt	Ch
GUE-5	-2.481191	47.342346	Dyke	Medium-grained (2mm), isotropic		Ms>>Bt	Ch+
GUE-16	-2.546417	47.291733	Dyke	Fine-grained (1-2mm), isotropic		Ms=Bt	
GUE-19a	-2.520933	47.356367	Dyke	Aplitic texture (0.5-1mm), shear zone	++	Ms>Turm>Grt	Ab+
GUE-19b	-2.520933	47.356367	Dyke	Aplitic texture (0.5-1mm), shear zone	++	Ms>Bt >Turm	Ab
GUE-20	-2.544000	47.366067	Dyke	Aplitic texture (0.5-1mm), isotropic		Ms	Ab-?

Table 2

[Click here to download Table: Table_2_Ballouardetal.docx](#)

Laser-ablation system ESI NWR193UC

Laser type/wavelength	Excimer 193 nm
Pulse duration	< 5 ns
Energy density on target	~ 7 J/cm ²
ThO ⁺ /Th ⁺	< 0.5%
He gas flow	~ 800 ml/min
N ₂ gas flow	4 ml/min
Laser repetition rate	3-5 Hz (zircon); 1-2 Hz (monazite)
Laser spot size	26-44 μm (zircon); 20 μm (monazite)

ICP-MS Agilent 7700x

RF power	1350 W
Sampling depth	5.0-5.5 mm (optimised daily)
Carrier gas flow (Ar)	~ 0.85 l/min (optimized daily)
Coolant gas flow	16 l/min
Data acquisition protocol	Time-resolved analysis
Scanning mode	Peak hopping, one point per peak
Detector mode	Pulse counting, dead time correction applied, and analog mode when signal intensity > ~ 10 ⁶ cps
Isotopes determined	²⁰⁴ (Hg + Pb), ²⁰⁶ Pb, ²⁰⁷ Pb, ²⁰⁸ Pb, ²³² Th, ²³⁸ U
Dwell time per isotope	10 ms (30 ms for ²⁰⁷ Pb)
Sampler, skimmer cones	Ni
Extraction lenses	X type

Table 3
[Click here to download Table: Table_3_Ballouardetal.docx](#)

Sample		GUE-11	GUE-12	GUE-13	GUE-14	GUE-15	GUE-17	GUE-3	GUE-6	GUE-8	GUE-1	GUE-2	GUE-9	GUE-18	GUE-21	GUE-4	GUE-7	GUE-10	GUE-5	GUE-16	GUE-20	GUE-19a	GUE-19b
Facies	Root	Root	Root	Root	Root	Root	Root	Ms-Bt	Ms-Bt	Ms-Bt	Ms-Turm	Ms-Turm	Ms-Turm	Ms-Turm	Ms-Turm	Fine	Fine	Fine	Dyke	Dyke	Dyke	Dyke	Dyke
SiO ₂	wt.%	72.9	74.2	72.8	72.3	71.6	73.6	72.5	72.5	73.3	73.2	73.5	72.9	73.7	69.8	72.1	72.3	71.8	73.4	72.9	75.3	74.4	74.1
Al ₂ O ₃	wt.%	14.76	14.50	15.27	15.34	15.04	15.01	14.95	15.43	14.97	14.66	15.01	15.27	14.81	16.11	15.04	14.92	15.18	14.28	14.79	14.01	15.20	15.14
Fe ₂ O ₃	Wt.%	0.45	0.73	0.59	0.87	1.16	0.22	0.68	0.38	0.78	0.52	0.67	0.45	0.71	0.81	0.96	0.92	0.99	0.53	0.51	0.26	bdl	0.36
MnO	Wt.%	0.01	0.02	0.01	0.01	0.01	0.01	0.01	0.01	0.01	0.01	0.02	0.01	0.02	0.01	0.01	0.01	0.01	0.01	0.01	0.01	0.01	0.03
MgO	Wt.%	0.14	0.16	0.16	0.24	0.32	0.07	0.20	0.15	0.24	0.16	0.15	0.16	0.21	0.22	0.24	0.26	0.30	0.12	0.14	0.06	bdl	0.05
CaO	Wt.%	0.71	0.48	0.59	0.83	0.82	0.62	0.57	0.46	0.75	0.43	0.40	0.62	0.59	0.83	0.78	0.80	0.73	0.55	0.71	0.21	0.37	0.27
Na ₂ O	Wt.%	4.40	4.00	4.05	3.54	3.85	3.83	3.79	3.73	4.01	4.18	4.51	4.07	3.66	3.28	3.78	3.61	3.26	3.77	3.93	4.68	8.71	7.10
K ₂ O	Wt.%	4.01	4.08	4.65	4.70	4.59	5.03	4.61	4.57	4.44	4.03	3.51	4.26	4.51	6.64	4.61	4.93	4.94	5.11	5.14	3.63	0.42	1.29
TiO ₂	Wt.%	0.07	0.09	0.09	0.15	0.18	0.06	0.12	0.12	0.10	0.08	0.06	0.11	0.10	0.11	0.12	0.15	0.16	0.06	0.08	0.02	bdl	bdl
P ₂ O ₅	Wt.%	0.16	0.25	0.14	0.25	0.23	0.22	0.23	0.23	0.23	0.24	0.29	0.21	0.35	0.59	0.25	0.22	0.23	0.18	0.25	0.14	0.23	0.19
LOI	Wt.%	0.94	0.95	0.79	1.00	0.89	0.05	1.14	1.54	0.98	1.10	1.09	1.19	1.25	1.09	1.04	0.74	1.34	0.63	0.67	0.84	0.39	0.80
Total	Wt.%	98.51	99.47	99.11	99.27	98.69	98.75	98.83	99.15	99.79	98.57	99.19	99.23	99.86	99.49	98.95	98.83	98.93	98.63	99.16	99.18	99.72	99.27
Cs	ppm	8	18	10	6	14	5	35	16	31	77	95	26	50	88	24	25	16	17	11	28	11	36
Rb	ppm	202	271	223	195	230	218	353	239	251	357	365	244	384	459	245	293	252	266	222	325	14	150
Sr	ppm	139	76	106	161	212	125	121	145	147	75	46	163	113	187	134	114	119	129	183	17	15	16
Ba	ppm	243	153	191	296	411	241	215	284	288	133	57	269	185	362	293	294	339	279	346	13	4	8
Be	ppm	5.7	11.0	7.0	3.9	9.2	9.2	18.4	11.3	13.7	18.7	12.9	15.0	34.5	6.0	15.4	9.8	9.2	24.0	12.6	131.3	129.3	158.5
Y	ppm	6.7	4.5	5.5	7.6	7.7	9.7	5.9	7.2	6.6	5.1	3.8	6.3	7.7	9.1	7.6	5.1	6.0	4.1	5.9	2.2	2.4	1.8
Zr	ppm	33	32	22	58	81	37	45	46	46	30	19	41	38	50	49	61	67	20	48	13	20	23
Hf	ppm	1.19	1.10	0.77	1.77	2.46	1.37	1.54	1.54	1.53	1.26	0.96	1.44	1.41	1.78	1.65	2.00	2.03	0.73	1.70	1.10	1.30	1.46
Nb	ppm	4.68	7.75	6.34	7.96	8.61	10.64	6.39	6.70	5.70	6.81	10.57	6.51	11.39	11.09	8.03	5.67	6.66	4.95	7.02	8.63	1.59	11.14
Ta	ppm	0.61	1.45	0.80	0.64	1.55	1.76	1.85	1.48	1.32	3.41	3.31	1.44	3.97	5.19	1.73	0.97	1.03	1.36	1.27	3.85	1.59	4.23
Th	ppm	2.64	3.72	1.97	5.24	9.15	2.20	3.46	3.52	3.14	2.59	1.44	3.04	2.94	3.59	3.89	5.63	6.36	1.49	5.49	0.29	0.59	0.61
U	ppm	2.35	3.99	2.74	2.44	4.75	4.02	3.35	4.24	6.42	2.90	1.71	2.41	3.09	4.05	5.98	7.24	3.78	6.21	3.64	1.63	1.96	1.87
Pb	ppm	73	41	74	68	77	83	54	68	65	61	41	73	66	92	55	44	52	76	85	42	15	15
V	ppm	1.9	1.7	2.8	4.2	8.2	1.0	3.9	4.3	3.5	2.2	1.4	3.8	4.5	3.7	4.0	3.5	5.0	1.1	2.2	bdl	bdl	bdl
Ni	ppm	bdl	bdl	bdl	bdl	bdl	bdl	bdl	bdl	bdl	bdl	bdl	10.0	bdl	bdl	bdl	bdl	bdl	bdl	bdl	bdl	bdl	bdl
Cr	ppm	4.6	12.2	9.0	6.3	17.2	bdl	9.9	11.0	15.9	10.3	5.7	25.7	10.7	13.9	14.9	16.7	5.5	36.3	5.3	5.1	4.1	bdl
Co	ppm	0.5	0.4	0.6	0.6	1.4	bdl	0.8	1.3	0.8	bdl	bdl	0.5	0.8	0.9	0.8	0.8	1.1	0.4	bdl	bdl	bdl	bdl
Cu	ppm	bdl	bdl	bdl	bdl	bdl	bdl	bdl	bdl	bdl	bdl	bdl	bdl	bdl	bdl	bdl	bdl	bdl	bdl	bdl	bdl	bdl	bdl
Zn	ppm	24	45	33	35	52	14	48	27	48	31	57	25	44	52	54	69	56	30	23	23	bdl	32
Ga	ppm	22.4	22.4	24.9	23.4	26.9	21.8	26.2	25.9	24.0	25.1	30.8	25.8	25.8	31.7	26.6	29.1	25.7	21.5	20.0	23.7	18.8	25.4
Sn	ppm	7.1	15.2	9.2	9.2	11.1	9.2	20.8	15.5	14.1	31.6	79.9	16.7	38.3	102.3	16.8	16.1	11.0	12.4	6.3	19.7	2.9	32.6
W	ppm	0.85	2.10	0.98	3.17	2.47	1.65	1.12	1.18	1.09	1.69	1.92	1.00	1.57	2.87	1.77	0.86	1.82	1.03	1.96	0.51	bdl	0.44
Bi	ppm	1.7	0.7	1.9	0.1	0.6	2.7	1.7	1.6	1.6	2.3	1.7	1.7	1.8	0.5	1.9	0.9	1.2	3.5	1.0	0.4	0.6	0.7
Cd	ppm	0.1	bdl	bdl	0.7	0.1	0.4	bdl	bdl	0.1	bdl	0.2	bdl	0.3	0.2	0.1	bdl	0.1	0.4	0.3	0.2	0.3	0.2
Ge	ppm	1.2	1.6	1.2	1.2	1.4	1.5	1.6	1.3	1.4	1.8	2.2	1.4	1.9	2.0	1.3	1.2	1.2	1.5	1.5	2.4	2.7	2.6
La	ppm	8.04	9.26	5.73	13.71	19.08	6.06	9.50	10.10	9.00	8.00	4.43	9.04	8.48	9.10	10.54	13.88	14.91	3.94	10.39	1.28	1.65	1.08
Ce	ppm	15.55	17.96	11.33	26.65	36.36	11.52	18.84	19.86	17.42	15.58	8.74	17.51	16.61	18.23	20.55	27.54	28.75	7.82	19.49	2.34	2.86	1.95
Pr	ppm	1.69	1.98	1.26	2.90	3.93	1.23	2.09	2.19	1.95	1.71	0.94	1.92	1.83	2.08	2.27	3.06	3.18	0.88	2.06	0.25	0.28	0.20
Nd	ppm	6.85	7.77	5.08	11.58	15.65	4.93	8.50	8.85	7.92	6.89	3.66	7.75	7.65	8.81	9.15	12.42	12.80	3.60	8.19	0.89	0.95	0.76
Sm	ppm	1.73	1.68	1.34	2.42	3.31	1.35	2.19	2.23	1.97	1.55	0.92	1.97	1.99	2.46	2.30	3.01	2.88	0.99	1.90	0.24	0.27	0.24
Eu	ppm	0.60	0.38	0.44	0.55	0.85	0.53	0.63	0.74	0.68	0.37	0.20	0.75	0.54	0.86	0.67	0.68	0.61	0.58	0.65	0.08	0.09	0.09
Gd	ppm	1.65	1.27	1.30	1.82	2.46	1.38	1.80	2.12	1.81	1.32	0.81	1.80	1.89	2.46	2.08	2.47	2.32	0.95	1.62	0.29	0.27	0.23
Tb	ppm	0.26	0.18	0.21	0.28	0.34	0.27	0.26	0.31	0.27	0.20	0.13	0.27	0.29	0.37	0.32	0.31	0.32	0.15	0.24	0.06	0.05	0.05
Dy	ppm	1.35	0.88	1.09	1.43	1.59	1.64	1.19	1.54	1.31	0.99	0.68	1.34	1.51	1.87	1.59	1.26	1.41	0.81	1.21	0.33	0.34	0.26
Ho	ppm	0.21	0.13	0.16	0.22	0.23	0.28	0.18	0.23	0.20	0.15	0.11	0.20	0.23	0.27	0.23	0.16	0.18	0.12	0.17	0.06	0.06	0.05
Er	ppm	0.50	0.35	0.40	0.58	0.58	0.74	0.43	0.53	0.48	0.38	0.28	0.47	0.56	0.65	0.53	0.35	0.41	0.30	0.45	0.15	0.16	0.13
Tm	ppm	0.07	0.05	0.05	0.08	0.08	0.11	0.06	0.07	0.07	0.05	0.04	0.07	0.08	0.09	0.07	0.04	0.06	0.04	0.06	0.03	0.03	0.03
Yb	ppm	0.42	0.38	0.34	0.53	0.51	0.71	0.39	0.44	0.41	0.35	0.30	0.41	0.48	0.52	0.44	0.26	0.38	0.28	0.41	0.18	0.22	0.20
Lu	ppm	0.05	0.05	0.05	0.07	0.07	0.10	0.05	0.06	0.06	0.05	0.04	0.05	0.07	0.08	0.06	0.04	0.06	0.04	0.06	0.02	0.03	0.03
A/NK		1.28	1.32	1.31	1.41	1.33	1.28	1.33	1.39	1.31	1.30	1.34	1.35	1.36	1.28	1.34	1.32	1.42	1.22	1.23	1.20	1.03	1.16
A/CNK		1.15	1.22	1.2	1.24	1.18	1.17	1.22	1.29	1.17	1.22	1.26	1.23	1.24	1.14	1.19	1.17	1.26	1.12	1.28	1.17	0.98	1.12

Table 4

[Click here to download Table: Table_4_ballouardetal.docx](#)

Sample	Rb (ppm)	Sr (ppm)	$^{87}\text{Rb}/^{86}\text{Sr}$	$^{87}\text{Sr}/^{86}\text{Sr}$	\pm	$(^{87}\text{Sr}/^{86}\text{Sr})$ 310 Ma	Sm (ppm)	Nd (ppm)	$^{147}\text{Sm}/^{144}\text{Nd}$	$^{143}\text{Nd}/^{144}\text{Nd}$	\pm	ϵNd (310 Ma)	T_{DM}^*
GUE-3	353	101	10.2	0.759868	11	0.7149	2.0	8.1	0.149821	0.512081	5	-9.0	1736
GUE-4	245	131	5.4	0.741854	11	0.7179	2.3	9.3	0.147638	0.512088	6	-8.8	1718
GUE-5	266	121	6.4	0.744704	12	0.7165	0.9	3.5	0.163489	0.512128	6	-8.6	1707
GUE-8	251	147	5.0	0.741599	11	0.7197	2.1	8.5	0.149165	0.512099	5	-8.6	1707
GUE-15	230	197	3.4	0.729724	10	0.7148	3.1	15.3	0.123199	0.512089	5	-7.8	1642

Table 5

[Click here to download Table: Table_5_ballouardetal.docx](#)

	Less differentiated GUE-15 sample	More differentiated GUE-12 sample			Segregate composition
		Measured	Computed	Difference	
SiO ₂	71.60	74.21	74.07	0.140	55.52
Al ₂ O ₃	15.04	14.50	14.35	0.151	19.54
Fe ₂ O ₃	1.16	0.73	0.53	0.195	5.23
MgO	0.32	0.16	0.21	-0.054	1.01
CaO	0.82	0.48	0.42	0.058	3.41
Na ₂ O	3.85	4.00	3.92	0.080	3.40
K ₂ O	4.59	4.08	3.98	0.097	8.54
TiO ₂	0.18	0.09	0.13	-0.040	0.51
P ₂ O ₅	0.23	0.25	0.02	0.232	1.61
Segregating minerals, Wt.%					
		Kfs	44.5		
		Bt	21.1		
		An20	30.7		
		Ap	3.7		
Amount of solid segregate removed, wt.%			13.3		
Sum residuals squared ΣR^2			0.16		